

# 1 Controls of the Latitudinal Migration of the Brazil-Malvinas

## 2 Confluence described in MOM6-SWA14

3 Nicole Cristine Laureanti<sup>1,2,3</sup>, Enrique Curchitser<sup>1</sup>, Katherine Hedstrom<sup>4</sup>, Alistair Adcroft<sup>5</sup>, Robert  
4 Hallberg<sup>6</sup>, Matthew J. Harrison<sup>6</sup>, Raphael Dussin<sup>7</sup>, Sin Chan Chou<sup>3</sup>, Paulo Nobre<sup>3</sup>, Emanuel Giarolla<sup>3</sup>  
5 and Rosio Camayo<sup>3</sup>

6 <sup>1</sup>Department of Environmental Sciences, Rutgers, The State University of New Jersey, New Brunswick, NJ, USA

7 <sup>2</sup>Potsdam Institute for Climate Impact Research, Potsdam, BB, Germany.

8 <sup>3</sup>National Institute for Space Research (INPE), Cachoeira Paulista, SP, Brazil

9 <sup>4</sup>College of Fisheries and Ocean Sciences, University of Alaska Fairbanks, Fairbanks, AK, USA

10 <sup>5</sup>Princeton University, Princeton, NJ, USA

11 <sup>6</sup>NOAA/OAR/Geophysical Fluid Dynamics Laboratory, Princeton, NJ, USA

12 <sup>7</sup>UCAR, Boulder, CO, USA

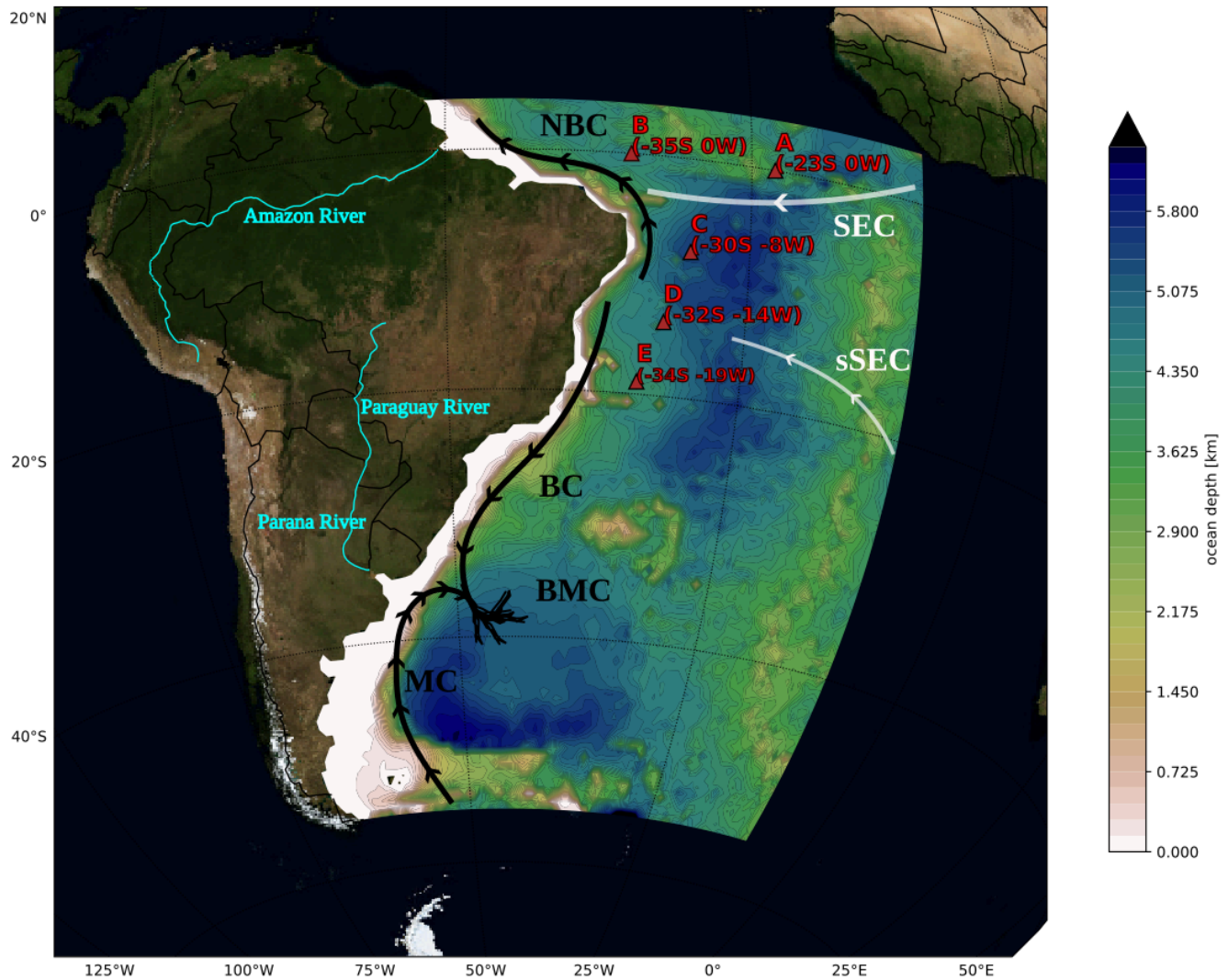
13 *Correspondence to:* Nicole C. Laureanti (nicole.laureanti@pik-postdam.de)

14 **Abstract.** The distribution and productivity of nutrients, eddy formation, energy dissipation, and other ocean properties are  
15 influenced by the variability of Western Boundary Currents (WBCs). In the Southwestern Atlantic, the key features are the  
16 Brazil-Malvinas Confluence (BMC) and the North of Brazil Current (NBC). This work investigates them using a 20-year  
17 high-resolution ocean model simulation with the Modular Ocean Model version 6 (MOM6) 1/14° configuration of the  
18 Southwestern Atlantic (SWA). The results reveal a significant deviation in the path and trends of volume transport of the  
19 WBCs over the decades. The BMC adjacent region gets saltier and warmer, with increased kinetic energy and transport.  
20 Although transport trends in the NBC indicate reduced transport, this results from weaker wind forcing, which reduces the  
21 Mixed Layer Depth (MLD) in the simulation and the subsurface transport in the region. The warming in the Brazil Current  
22 region triggers a stronger southward flow, resulting in a southward shift of  $0.93^\circ \pm 0.08$  of latitude/decade in the BMC  
23 separation. Working against this flow, the propagation of the Kelvin Waves from the Eastern Pacific Ocean induces a  
24 northern shift of the BMC, revealed by topographic Kelvin Waves in the spectral analysis. This Pacific-Atlantic inter-basin  
25 relation indicated here underscores the importance of propagating Pacific disturbances into the region to maintain the  
26 positioning of the BMC and its properties under a warming Atlantic Ocean.

27 **Keywords:** Western Boundary Currents; Brazil-Malvinas; climate trends; Kelvin topographic waves

## 28 1 Introduction

29 Recent studies have revealed a relationship between the Southwestern Atlantic Ocean and extreme precipitation events in  
30 South America (Rodrigues et al., 2019; Pezzi et al., 2022; Laureanti et al., 2024). The investigation of this ocean circulation  
31 was also motivated by oil spills and other accidents polluting the Brazilian coastline, striking important naturally preserved  
32 areas (Nobre et al., 2022). Climate studies in the region have focused on heat budgets and trends (Muller et al., 2021; Franco  
33 et al., 2020). Improving the description of the ocean circulation features in this region can result in a better understanding of  
34 the dynamics, including even that of the CO<sub>2</sub> distribution (Valerio et al., 2021; Bonou et al., 2016). To extend the knowledge  
35 of these features, this work focuses on investigating the variability and trends of the Western Boundary Currents (WBCs) in  
36 the Southwestern Atlantic Ocean.



37

38 **Figure 1: The Southwestern Atlantic simulation domain. The arrows illustrate near-surface currents: from north to south, the**  
39 **South Equatorial Current (SEC) and its southern branch (sSEC), the North Brazil Current (NBC), the Brazil Current (BC), the**  
40 **Malvinas Current (MC) and the Brazil-Malvinas Confluence (BMC). The Western Boundary Currents (WBCs) are in black. The**  
41 **shaded colors indicate the topography in the Southwestern Atlantic Ocean used in MOM6 simulations. The locations of the 5**  
42 **PIRATA buoys with observational data are in red. The locations of the major rivers in this domain are shown in blue. Satellite**  
43 **images from Blue Marble: Next Generation define the terrain contours by NASA Earth Observatory.**

44 The Atlantic Ocean is an energetic region with both surface and undercurrents between the Brazilian eastern coast and the  
45 African western coast. Figure 1 illustrates the sea surface currents in this region, including the North Brazil Current (NBC)  
46 and the Brazil Current (BC), whose flow is maintained by the southern branch of the South Equatorial Current (sSEC). The  
47 sSEC redirects toward South America after originating in the Angola Gyre off the Western African Coast. The BC and the  
48 Malvinas Current (MC) confluence at a southward region (Garzoli and Bianchi, 1987; Goni et al. 2011; Combes and Matano,  
49 2014b; Barré et al. 2006; Ferrari et al. 2017; Artana and Provost 2023), forming the Brazil-Malvinas Confluence (BMC).  
50 This region experiences intense oceanic mesoscale activity due to the retroflexion of these currents (Oliveira et al., 2009).  
51 The MC originates in higher latitudes and flows northward, driven by the Antarctic Circumpolar Current (ACC) (Combes  
52 and Matano, 2014b). Meanwhile, the NBC encounters the continental shelf in Northwestern Brazil, where its retroflexion  
53 generates eddy propagation (Bueno et al., 2022; Garzoli et al., 2004). These are recognized as WBCs, as they path is set  
54 along the coastline, comprising unique dynamic properties and interactions with the continental shelf, a common  
55 characteristic in the BC, MC, and NBC.

56

57 The wind plays a dominant role in the variability of the WBCs (Wunsch and Ferrari, 2004). It impacts the mesoscale  
58 structure within the Gulf Stream, which is a WBC in the Northwestern Atlantic Ocean, affecting the Mean Kinetic Energy  
59 (MKE) to Eddy Kinetic Energy (EKE) conversions along the coast (Kang et al., 2016). The wind contribution to the BMC  
60 variability can be explained by the frequent passage of atmospheric fronts at those latitudes that alter the predominant wind  
61 direction and cause sudden reversal of the currents throughout the water column (Campos et al., 2013; Lago et al., 2019).  
62 Furthermore, specific analysis of the MC near the Patagonian shelf has demonstrated its modulation by wind stress (Guerrero  
63 et al., 2014; Palma et al., 2004; Lago et al., 2019). Additionally, winds also influence the Plata River discharge impacting the  
64 BC flow (Piola et al., 2005; Campos et al., 2013). Northwesterly wind-stress anomalies commonly induce heavy runoff over  
65 summer, spreading river plumes meridionally. During wintertime, strong southwesterly winds intensify a northward current,  
66 causing freshwater discharges from the La Plata Basin to move northward. The seasonality of the atmospheric patterns also  
67 contributes to precipitation inputs, which has been considered a contributor to ocean variability (Campos et al., 2013; Lago et  
68 al., 2019; Palma et al., 2004). An interannual variability influence near the La Plata Basin is also evident, where the El  
69 Niño-Southern Oscillation (ENSO) impacts freshwater discharges (Combes and Matano, 2018). In addition, some studies  
70 have recognized the contribution of the South Atlantic Subtropical High (SASH) and the Intertropical Convergence Zone  
71 (ITCZ) for the NBC variability. The SASH is the lower-level atmospheric dominant feature of the SEC, impacting the  
72 SEC-NBC transport, while the ITCZ predominantly contributes to the Equatorial currents (Lumpkin and Garzoli, 2005;

73 Valerio et al., 2021). Important features related to its variability relate to the propagation of eddies in the NBC retroflexion,  
74 which results in a deviation of its natural path from 4°N to 8°N (Bueno et al., 2022; Valerio et al., 2021).

75

76 The highly energetic activity imposes challenges for diagnosing SST in places adjacent to WBC in General Circulation  
77 Models (GCMs) (Stock et al., 2015; Adcroft et al., 2019). The oceanic grid resolution is key for simulating the physical  
78 processes, as it determines the range of perturbations reproduced by the model (Adcroft et al., 2019; Hallberg, 2013;  
79 Chassignet and Xu, 2021). At least a 1/8° resolution is required to explicitly capture the mesoscale baroclinicity in the  
80 Southwestern Atlantic, while a resolution higher than 1/25° is recommended for continental shelf regions (Hallberg, 2013).  
81 In addition, using a high-resolution ocean bathymetry induces better heat distribution by ocean currents (Griffies et al.,  
82 2015). Regional numerical simulations can provide specific diagnostics, including distinct driving mechanisms for shelf  
83 circulation. For instance, studies conducted by Palma et al. (2004, 2008) explored the significance of wind and tidal motion  
84 in the Patagonian Shelf. The findings indicated that south of 40°S, circulation is primarily influenced by semidiurnal tidal  
85 mixing (M2, S2, N2), wind, and the MC. The tidal mixing enhances bottom friction that balances the energy input by the  
86 wind stress. Similar outcomes were described in a high-resolution simulation using the Regional Ocean Modelling System  
87 (ROMS) (Combes and Matano, 2014a). Local winds contribute significantly to the shelf variability, but adding tides is  
88 crucial to replicating the mixing near the coastal region accurately. The MC's transport is highly correlated with the  
89 upwelling at the Patagonian shelf break and exhibits an out-of-phase relationship with the BC (Combes and Matano, 2014a).

90

91 There are also important WBCs relations driven by the proximity to the coastal slopes (Hughes et al., 2019). The internal  
92 variability of the currents and transport in the WBCs offers a broader number of dynamic interactions, different from those in  
93 the open ocean. Tropical waves from the Pacific follow the western South American coastline, propagate, and contribute to  
94 the coastal dynamics in the Southwest Atlantic Ocean. Poli et al. (2022) reveal that Kelvin wave dispersion and Rossby wave  
95 propagation from the Madden-Julian Oscillation are linked to the barotropic and baroclinic components of the coastal  
96 trapped waves in the Southwest Atlantic Ocean.

97

98 This study aims to extend our understanding of this region by simulating and evaluating the ocean circulation. The relevance  
99 of this implementation to global climate studies is the focus on the WBCs, indicating their unique variability and potential  
100 drivers. Simulating the Southwestern Atlantic WBCs with a high-resolution framework allows for determining meaningful  
101 characteristics of the variability of the mesoscale circulation.

102 This article is organized as follows: The first two Sections detail the model setup and the datasets. The results initially focus  
103 on evaluating surface features and vertical structures by comparing them with local observational data in Section 3.1. The  
104 analysis discusses the characteristics of the meso- and large-scale circulation within the domain, assessing the contribution of  
105 winds and ocean transport to the overall dynamics in the model. Section 3.2 discusses the seasonal variability and trends of  
106 the WBCs. In Section 3.3, we focus on the internal and external components of the variability of WBCs. The final section

107 contains the discussion and conclusions, offering an analysis of the variability of the WBCs circulation reproduced by the  
108 model.

## 109 **2 Model and Data**

### 110 **2.1 Model Description and Configuration**

111 The model used in this work is the Modular Ocean Model version 6, developed by the Geophysical Fluid Dynamics  
112 Laboratory (GFDL) from the National Oceanic and Atmospheric Administration (NOAA) (Adcroft et al., 2019). The model  
113 was designed to represent the ocean's general circulation. The version used in this paper is capable of running on regional  
114 configurations as a result of the implementation of open boundary conditions. The horizontal grid extends from longitude  
115 69°W to 9° W and from latitude 55°S to 5°N, at 1/14° resolution (approx. 7 km). The model domain uses the topography  
116 displayed in Figure 1. The ocean bathymetry was interpolated from a horizontal resolution of 450 meters from the General  
117 Bathymetric Chart of the Oceans (GEBCO) (Giribabu et al., 2023). The vertical discretization distributes 75 levels from 3  
118 meters up to 6,500 meters of depth, varying in thickness from 2 m near the surface up to 250 m in the deep ocean. The  
119 model uses the  $z^*$  vertical coordinate, which is a height-based coordinate rescaled with the free surface (Adcroft and  
120 Campin, 2004). Under this setup, the model simulation started on 1st January 1997 and ended on 31st December 2016, a  
121 total of 20 years. A test run made with the model with a hybrid vertical coordinate is also evaluated from 1997 until 2002, to  
122 verify impacts of the vertical discretization.

123

124 The model uses initial and boundary conditions data from GLORYS12v1 ocean reanalysis, developed by the Copernicus  
125 Marine Environment Monitoring Service (CMEMS), with a daily frequency and an 8-km resolution (1/12°) (Jean-Michel et  
126 al., 2021). The atmospheric forcing is the hourly reanalysis data from the European Centre for Medium-Range Weather  
127 Forecasts (ECMWF) fifth generation (ERA5) at 25 km (Hersbach et al., 2023). Ten tidal components from the global model  
128 of ocean tides TPXO (Egbert and Erofeeva, 2002) are used in the boundaries and internal domain to force the barotropic  
129 conditions through parametrization. The components are four semidiurnal (M2, S2, N2, and K2), four diurnal constituents  
130 (K1, O1, P1, Q1), and two long-period constituents (Mm and Mf). The freshwater discharge is from the Global Flood  
131 Awareness System (GloFAS) reanalysis dataset (Zsoter et al., 2021). To assimilate natural conditions, chlorophyll estimates  
132 from the Sea-viewing Wide Field-of-view Sensor (SeaWiFS-NASA) (NASA, 2018) are inserted in the opacity scheme to  
133 modify the estimate of the atmospheric radiation reaching the deepest layers. The MOM6 schemes are based on the physical  
134 ocean model configuration of Ross et al. (2023). Parameterizations include the convection Energetic Planetary Boundary  
135 Layer (ePBL) approximation (Reichl and Hallberg, 2018), the Fox-Kemper restratification for the mixing layer (Fox-Kemper  
136 et al., 2011), while astronomical tides and the Kappa-shear scheme (Jackson et al., 2008) induces interior and bottom mixing,  
137 respectively.

## 138 2.2 Data for Validation

139 The 20-year simulation is assessed by comparing mean fields with observational data. The World Ocean Atlas (WOA)  
140 temperature and salinity climatology (Locarnini et al., 2019; Zweng et al., 2019) and the Surface Mixed Layer Depth (MLD)  
141 climatology from de Boyer Montégut et al. (2004) correspond to the datasets of coarser resolution with a  $1^\circ$  resolution. A  
142 local comparison relates the model results to the observational data from 4 buoys from the Pilot Research moored Array in  
143 the Tropical Atlantic (PIRATA) project (Servain et al., 1998). The dataset consists of time series and vertical profiles of  
144 temperature and salinity over the tropical Atlantic, with five moored buoys in the tropical Atlantic, two on the equator that  
145 have data from January 1998 to recent years, and the other three are placed southern, with measurements starting in August  
146 2005. The buoys are A:  $0^\circ\text{S } 23^\circ\text{W}$ , B:  $0^\circ\text{S } 35^\circ\text{W}$ , C:  $8^\circ\text{S } 30^\circ\text{W}$ , D:  $14^\circ\text{S } 32^\circ\text{W}$ , and E:  $19^\circ\text{S } 34^\circ\text{W}$  and their locations are  
147 shown in Figure 1. The GLORYS12v1 reanalysis, used as forcing and for comparison with model outputs, provides  
148 comparable results in high-resolution daily data. Besides the assimilative schemes, this reanalysis uses ERA-Interim and  
149 ERA5 data in the surface and the dynamical core from NEMO in 50 standard levels (Jean-Michel et al., 2021). The mean  
150 winds from ERA5 are compared against the  $0.125^\circ$  QuickSCAT (QSCAT) satellite data, available between 1999 and 2009  
151 (Hoffman and Leidner, 2005).

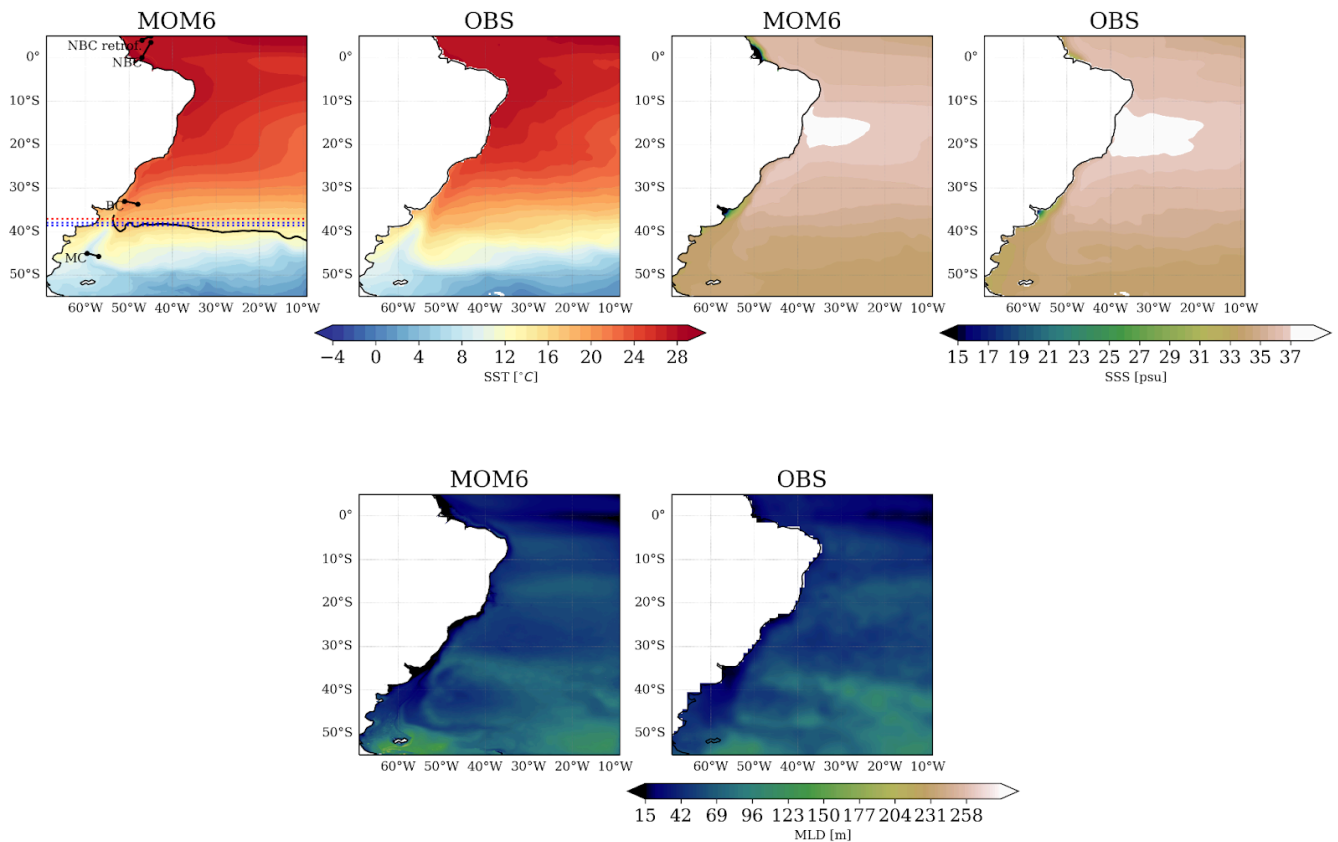
## 152 3 Results

### 153 3.1 Evaluation of the Simulation Mean State

#### 154 3.1.1 Ocean Surface

155 Surface variables often characterize the main features that develop in the ocean. Figure 2 displays the mean surface variables  
156 from model outputs compared to observations. The fields originate from different horizontal resolutions, with a coarser  
157 resolution for the observations, resulting in a lack of representation of higher-resolution structures, especially near the  
158 coastline. Overall, the results indicate a good representation of the mean state fields. The central South Atlantic is the region  
159 with the most similar SST patterns. The major differences appear in the open sea with colder SST in the eastern equatorial  
160 Atlantic in the model. The difference in the BMC is negative and less than  $1^\circ\text{C}$ , which is more accurate than the one obtained  
161 with the global  $1/4^\circ$  version of the model, with a positive bias greater than  $2^\circ\text{C}$ , using the same vertical model coordinate  
162 (Adcroft et al., 2019), highlighting the benefits of increasing the horizontal resolution.

163



164

165 **Figure 2: Sea Surface Temperature (top row), Salinity (middle row), and Mixed Layer Depth (bottom row), 20-year mean from the**  
 166 **simulation (left) and WOA observations (right). In (a), the illustrated black line is the 10°C isotherm at 200 m, where it meets with**  
 167 **the 1000 m isobath, an estimate proposed by Garzoli and Bianchi (1987) to indicate the BMC separation in the model. The dotted**  
 168 **curves represent the mean BMC separation using (red) GLORYS12v1 reanalysis and (blue) the obtained from satellite**  
 169 **observational sets by Goni et al. (2011).**

170

171 The model captures the development of the BMC, with the location of the temperature gradients in the region. The  
 172 northward propagation of surface cold waters through the MC ends at approximately 37°S. The confluence with the BC  
 173 appears within this region, which is close to estimates from observational data (Figure 1; Goni et al., 2011; Lumpkin and  
 174 Garzoli, 2011). A similar gradient is found in the observations, but cooler temperatures emerge near the La Plata Basin coast.  
 175 The model shows extra fresher waters near the La Plata and the Amazon Basins, indicating that the salinity is close to zero  
 176 downstream of the basins. The model presents less salty waters than the observations at around 10-20°S, which appears to be  
 177 related to the river discharges. However, the freshwater inputs look trapped in shallower depths on the coastline, and  
 178 according to the ocean circulation (Figure 1), the fresher water inputs flow south for the La Plata River and northwest for the  
 179 Amazon River. The MLD pattern diagnosed by the ePBL's model scheme is consistent with the patterns of the observations  
 180 despite the impacts of the river on the coastline circulation.

181

182 Contrasting patterns between the shallow and deepest regions appear from comparing the model seasonal averages with  
183 reanalysis from GLORYS12v1 with similar horizontal resolution (Jean-Michel et al., 2021). Figure 3 shows the sea surface  
184 density for each trimester, estimated by the equation of state for ocean models considering temperature and salinity (Wright,  
185 1997). There is a higher consistency in the seasonal density between the fields far from the coast. Some differences in  
186 temperature contours emerge in the northwestern and southwestern South Atlantic, where the model keeps colder equatorial  
187 waters during most seasons. Although the difference in the temperature field has maximum values of  $-1^{\circ}\text{C}$  to the south of  
188  $30^{\circ}\text{S}$ , especially during March to May (MAM) and June to August (JJA), it reproduces a weaker variance in the density field.  
189 The difference in density in the tropics is unrelated to the temperature variations and indicates the presence of freshwater  
190 inputs from the rivers, as indicated in Figure 2.

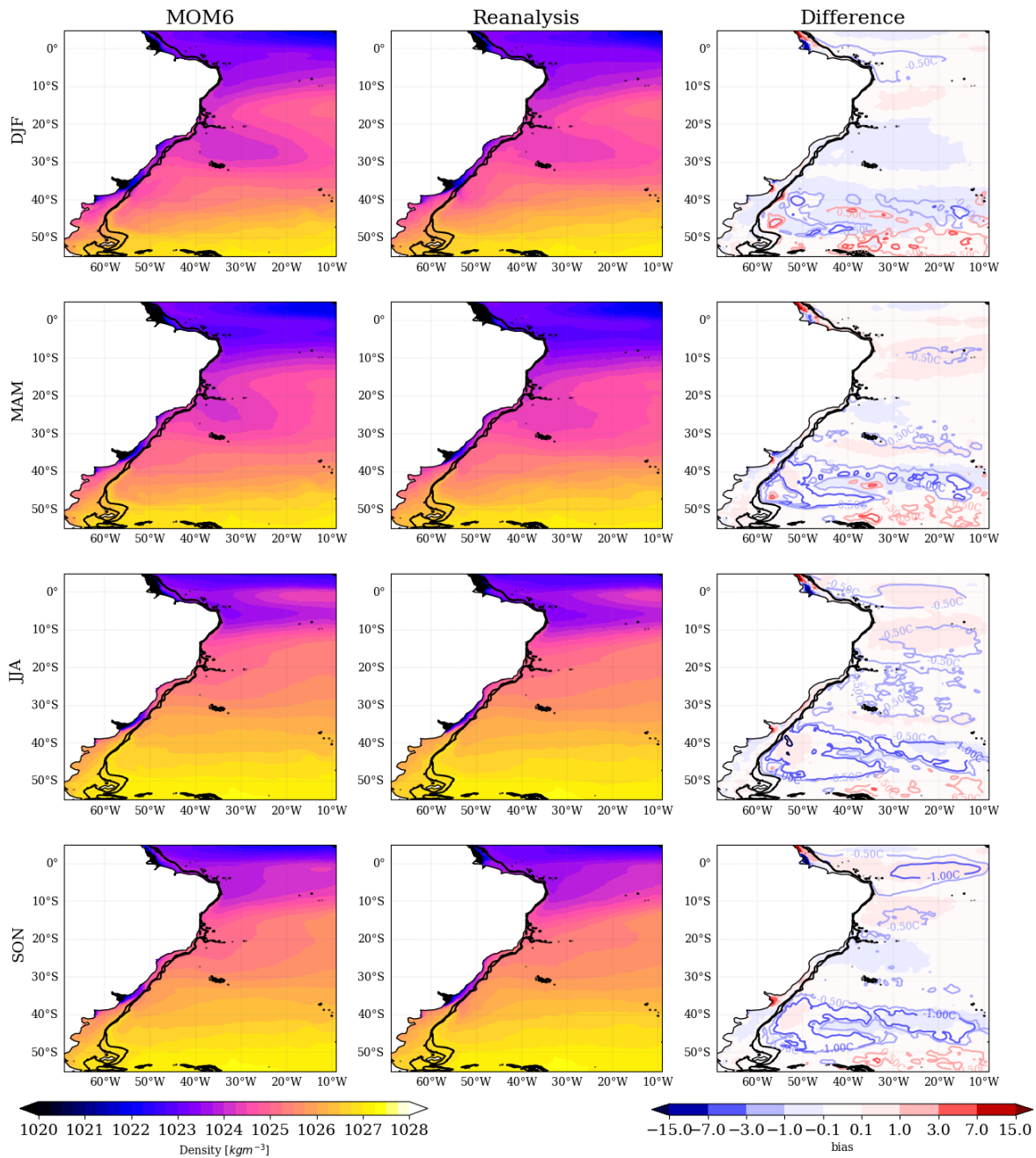
191

192 The most significant differences in density appear in the shallow areas in the Amazon region, which exhibits variability  
193 related to the river's seasonality. The contrasting heavy rainfall related to the ITCZ displacement is related to the region's  
194 variability (Valerio et al., 2021). It contributes significantly to the mean flow from December to February (DJF) until MAM,  
195 with fewer discharges during JJA and September to November (SON). The difference in the density fields (Figure 3)  
196 indicates that the model representation of the river discharges is more coherent during MAM, the period of higher freshwater  
197 discharge. The model's salinity distribution is counterbalanced in the other drier seasons, showing reduced salinity in the  
198 Amazon River basin and increased in the extreme northwest of the domain. Thus, deviations in the mixing of the river  
199 discharges imply the appearance of a core of higher density northwest of the domain and a lower density in the Amazon  
200 basin in Figure 3. The density is higher in the model when more saline waters than the reanalysis are found and lower when  
201 more fresher waters appear.

202

203 Like the Amazon, the river seasonality implies modifications in the river discharges in the La Plata Basin. The model  
204 overestimates the density downstream of the La Plata Basin due to more saline waters on the southwest coast, mostly during  
205 SON. During winter (JJA), strong runoff is enabled by the frequent passage of atmospheric systems when the intense rainfall  
206 and wind spread the freshwater discharges of the river plume (Campos et al., 2013; Lago et al., 2019; Piola et al., 2005).

207



208

209 Figure 3: Seasonal mean surface density for the MOM6 simulation, the reanalysis (GLORYS12v1) and error. Each row shows a  
 210 season, from the top to the bottom, DJF, MAM, JJA, and SON, marking the transition from austral summer to spring. The means  
 211 consider the period from 1997 until 2017. The contours in the right column show the temperature errors in the open ocean (depth  
 212  $\geq 1000$  m), with contours at  $\pm 0.5$ , 1.0, and 3.0°C. The thick black contours indicate the 200 and 1000 m isobaths.

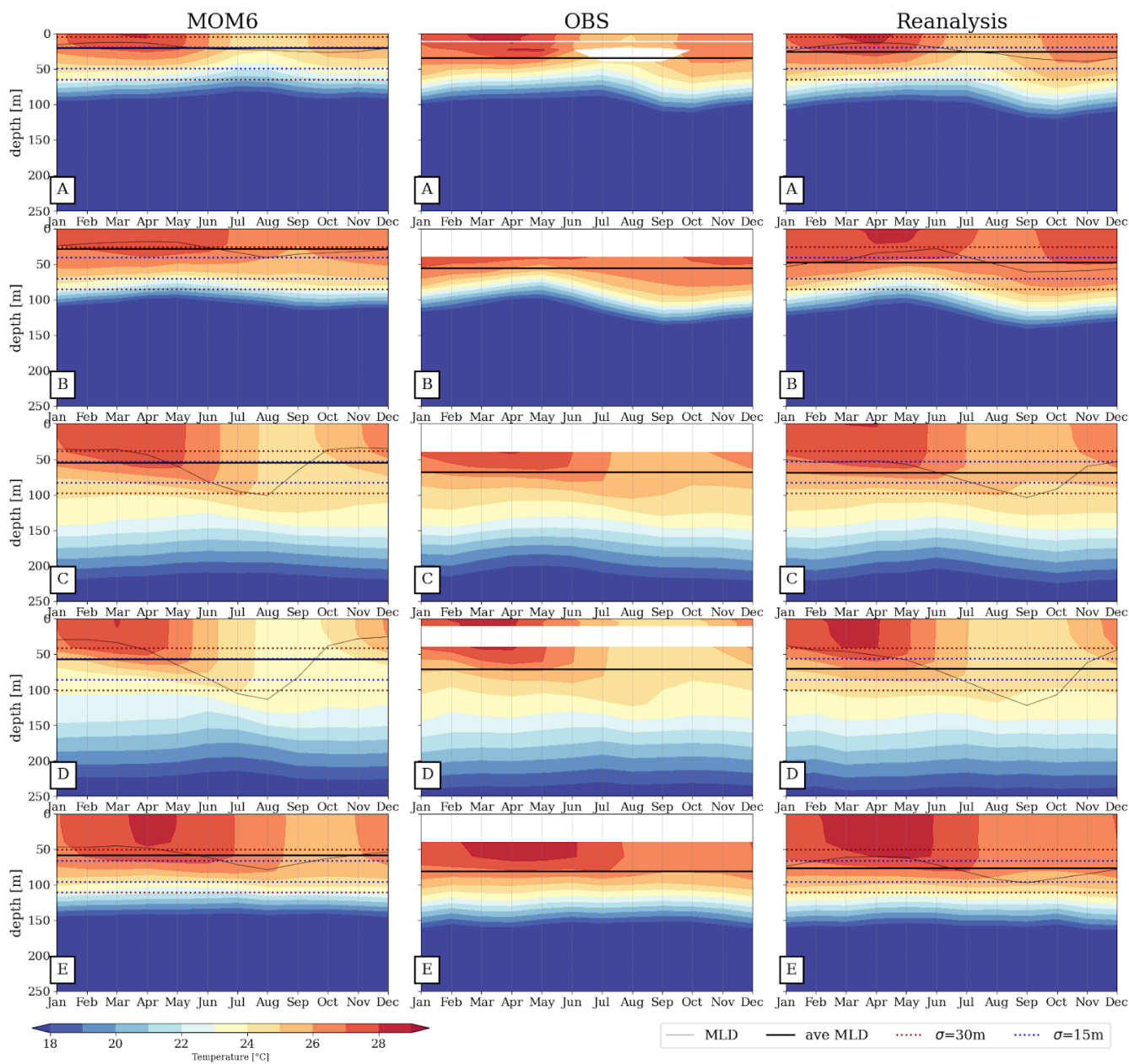
213

214 The importance of determining the advancement of freshwater plumes into the open ocean in both basins has been described  
215 in the literature (Valerio et al., 2021; Campos et al., 2013). Although the surface fields based on the 20-year model averages  
216 exhibited bias constrained by the coastline, the freshwater plumes accurately display the river seasonality. The river  
217 discharges simulated by the model represent the impact on the MLD seen in Figure 2. In addition, the salinity variations near  
218 the Amazon and La Plata basins also considerably impact the surface density comparable to the reanalysis (Figure 3).  
219 Although a similar resolution increases the consistency of the results in the basins, unbalanced freshwater amounts still  
220 occur. The results indicate that the amount of freshwater on the surface and the lower density contribute to less mixing in  
221 shallower depths. At higher depths, the similarity of the results, especially in MLD and density patterns, indicates that the  
222 unbalanced freshwater influences the appearance of local biases more strongly at the deltas of the Amazon and La Plata  
223 Rivers. However, there are still biases near the BMC and in tropical regions that may be due to other factors.

### 224 3.1.2 Vertical Structure of Temperature and Seasonal Variability

225 Profiles of potential temperature in Figure 4 characterize the vertical structure in the ocean model against the reanalysis and  
226 the PIRATA buoys observations. The depth of the 18°C isotherm compared to the buoys evidences the conformity in the  
227 vertical structure. The 18°C isotherm in the A and B observations shows deeper seasonal fluctuations during SON, so the  
228 model fails in reproducing the structure. During the warmer season, MAM, when the warmer waters reach deeper layers in  
229 the observations, the model remains cooler until the wintertime. This effect reduces the MLD in the model, which shows a  
230 30 m shallower MLD (Figure 4, right column) than the other datasets in the buoy sites (Figure 4, left and center). The  
231 difference is even more critical at the buoy B site, where the MLD is more than 30 m shallower in the model.

232

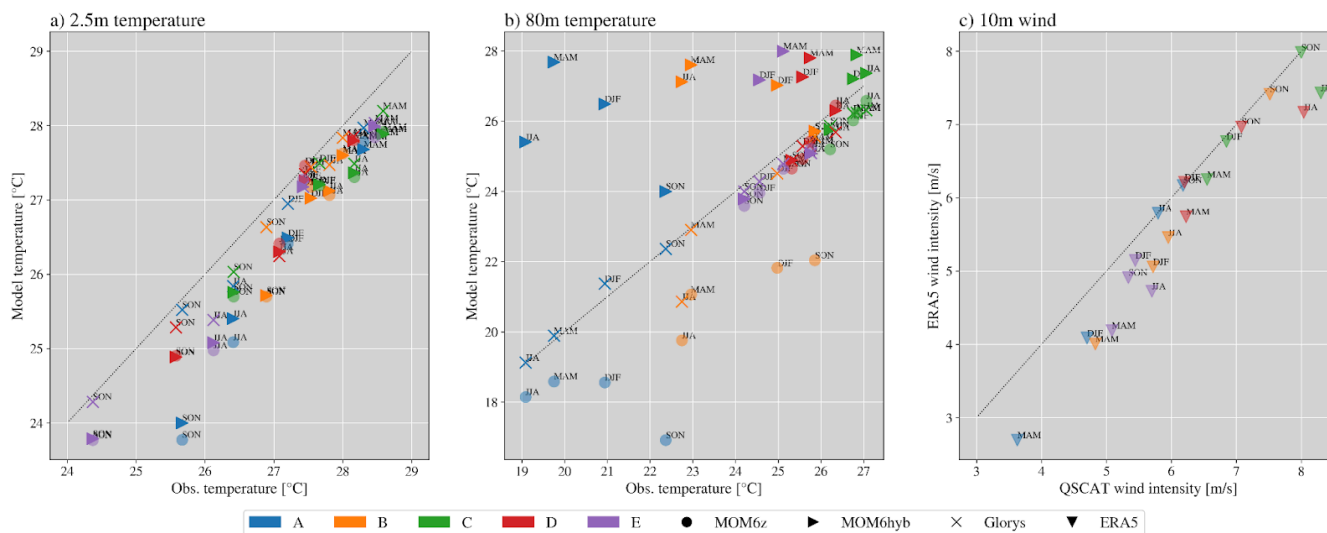


233

234 **Figure 4: Mean annual cycle of the vertical profile of temperature and MLD at PIRATA buoy sites. The colors display the**  
 235 **temperature, and the lines are the MLD. The letters identify the buoy sites from A to E. MOM6 outputs are on the left column,**  
 236 **observed data from the PIRATA buoys are in the center, and reanalysis products are on the right. The MLD for observation and**  
 237 **reanalysis are estimated with the  $\Delta T = 0.2^\circ\text{C}$  temperature threshold from a near-surface value and the 10 m. Missing data appears**  
 238 **at different depths in the observations and are shown in white. The dashed lines highlight depths above/below the mean**  
 239 **buoy-estimated MLD in blue with a difference of 15 m and in red 30 m.**

240

241 The temperature at shallow and deeper regions shown at the buoy sites in Figure 5 explains the reduced heat entrainment  
 242 from the surface layers in the model due to different factors. Near the surface, the model temperature is approximately  $\leq 1^\circ\text{C}$   
 243 lower than the reanalysis and the buoys through the seasons (Figures 3 and 5a). The model presents a well-defined seasonal  
 244 cycle near the surface (Figure 5a), when a warmer surface appears during MAM and cooler in JJA and SON. More  
 245 contrasting outliers are in the 80 m depth layer (Figure 5b), with the buoys in the tropical region revealing higher  
 246 temperatures obtained with the hybrid coordinate compared to the  $z^*$  coordinate. In the other buoy sites (C, D, and E), far  
 247 from the equatorial region where the water column is deeper (Figure 1), the model presents a reduced bias. Reproducing the  
 248 80 m temperature in the equatorial region is a challenge even in the reanalysis (Figure 5b). Compared to the model in  $z^*$ , the  
 249 observations at sites A and B present  $2^\circ\text{C}$  warmer temperatures during SON and  $1^\circ\text{C}$  warmer temperatures during DJF. This  
 250 divergence for site B starts in JJA, getting colder by more than  $2^\circ\text{C}$  than the observations in SON. For buoy A, the most  
 251 divergent seasons are SON and DJF.  
 252 The heat entrainment capability of the model in the equatorial region is enhanced by changing the vertical coordinate from  
 253  $z^*$  to the hybrid coordinate. This is shown by comparisons of the  $z^*$  and hybrid coordinates for the 5-year run (Figure 5b).  
 254 This vertical discretization allows the warmer structure at 80 m to be reproduced on SON, although the temperatures in other  
 255 seasons remain high. A more qualified description of these mechanisms and additional adjustments can be disclosed in the  
 256 following studies. For comparison, Supplementary Figure 1 shows that the temperature distribution remains the same for the  
 257 model in the  $z^*$  coordinate over the entire simulation period.



258

259 **Figure 5: Seasonal 2.5-m and 80-m temperatures and 10-m winds, compared against observations. The graphs display the**  
 260 **temperature at 2.5 m (a) and 80 m (b) for the model and reanalysis compared to PIRATE buoy observations. In (c), the**  
 261 **atmospheric forcing for the model, 10-m wind from ERA5, compared to QSCAT satellite observation (Hoffman and Leidner,**  
 262 **2005). Colors distinguish the buoy sites from A to E. The model data is plotted with two vertical discretizations: MOM6z takes the**  
 263  **$z$ -coordinate system and MOM6hyb uses a hybrid system. The same period of 5 years is considered for the model data. The**  
 264 **reanalysis from GLORYS12v1 is marked with crosses and ERA5 triangles. The seasons are named as DJF, MAM, JJA, and SON.**

266 The tendency of the model to underestimate the entrainment of seasonal heat at the equator indicates a concern about the  
267 ITCZ displacement. The latitudinal ITCZ displacement causes the most intensive surface heating during MAM (Valerio et  
268 al., 2021), reproduced with lower bias by the model considering observations (Figures 3 and 5a). This enables the  
269 development of stratification and heating of the deeper layer in the following seasons. However, although the model  
270 reproduces the warmer temperatures during MAM and JJA, the deeper layers remain cooler until SON (Figure 5b). This  
271 deviation indicates that although the model receives the seasonal heat at the surface, it gets under-mixed during the stratified  
272 period. In contrast, for the reanalysis and the hybrid MOM6 set-up to reproduce the heating and the accordant stratification  
273 structure during SON, the 80 m-depth waters are slightly warmer than the buoys for sites A and B.

274

275 The seasonal ITCZ displacement impacts wind speed in the buoy sites, which is a misleading diagnostic that can interfere  
276 with ocean currents and mixing. The model wind forcing (ERA5) is compared to QSCAT satellite observations in Figure 5c  
277 to observe this effect. Although the ITCZ depends most on the wind structure during DJF and MAM in the equatorial region,  
278 ERA5 wind is slower than the observations through all seasons. During the warm season, buoy sites A, B, and E present  
279 wind forcing almost 1 m/s slower. The wind pattern, which contributes to the vertical mixing, suggests that equatorial region  
280 temperature biases occur due to the lack of a wind-driven source.

281

282 The deviation of mixing temperature and freshwater in the adjacent layers can be a response to the vertical coordinate system  
283 (Figure 5b) and to the weaker ERA5 10m-wind, compared to the estimates from satellite observations (Figure 5c). The winds  
284 lead to less mixing in the bottom layers since it dissipates the wind stress, the main energy source to the currents, and  
285 subsequent horizontal transport. These factors can also contribute to the salinity differences in the northwestern part of the  
286 domain. Lighter density is placed in the Amazon Basin due to the weak zonal winds and a lack of mixing, resulting in the  
287 fresher water patterns in the surface. In turn, the lack of advection of freshwater results in salty and more dense waters ( $> 7$   
288  $\text{kgm}^{-3}$ ) in the northwest corner of the domain (Figure 3).

### 289 3.1.3 Meso- and Large-scale Circulation

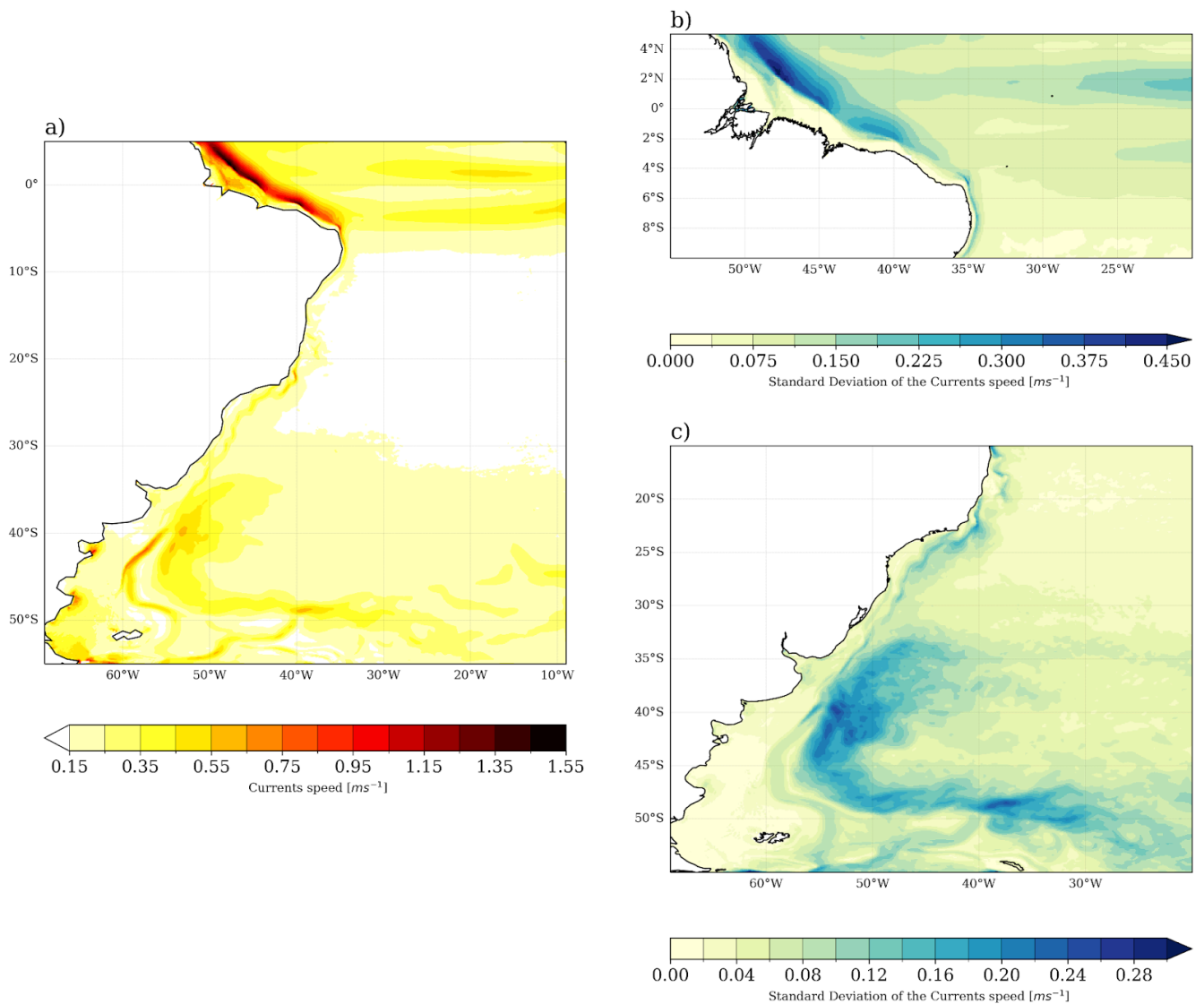
290 The ocean circulation comprises the distribution of the current speeds and energy, potentially related to the tracer exchanges  
291 in the domain. The analysis in this study allows the observation of meso- and large-scale circulation as represented by the  
292 model. The 20-year mean surface current speed model outputs in Figure 6a display the mean natural path of the main  
293 currents, depicted in Figure 1: SEC, NBC, BC, and the MC, distinguished from the mean flow. The BC is observed through  
294 the warm high-speed currents on the mid-western Atlantic flowing southward from  $20^{\circ}\text{S}$ . The MC surrounds the east of the  
295 Patagonian Shelf on the Argentinean coast south of  $40^{\circ}\text{S}$ , and the eastward flow in  $50^{\circ}\text{S}$  marks the origin of the South  
296 Atlantic Current. The mean speed field also allows the appearance of high-speed currents in the BMC, between  $35^{\circ}\text{S}$  and  
297  $45^{\circ}\text{S}$ . In the northwest, the flow of the NBC and the connection with the SEC is also pronounced. The NBC is north of  $5^{\circ}\text{N}$

298 and to the northwest. Thus, the model places the ocean currents that agree with the general location described by others  
299 (Lumpkin and Garzoli, 2005; Oliveira et al., 2009).

300

301 The current speed standard deviation for the two main WBCs reveals that the model can reproduce the variability of these  
302 features in various different shallow parts of the domain (Figure 6b and c). The NBC is the most prominent current in the  
303 domain, and the speed reaching 1.5 m/s and the standard deviation of 0.45 m/s indicate larger variability. This dynamic  
304 background induces the formation of mesoscale structures through the NBC retroflection (Bueno et al., 2022; Garzoli et al.,  
305 2004). Part of this variability is due to the topographic gradient but also induced by the seasonal cycle and the river  
306 discharges of the Amazon River. Another contributing factor is the SEC's high speed ( $> 0.45$  m/s) and deviation ( $> 0.15$  m/s)  
307 in equatorial waters. The SEC maintains East-West oceanic transport, suffering from the seasonal effect drift due to the trade  
308 winds, which decreases its intensity during DJF compared to JJA (Lumpkin and Garzoli, 2005). The propagation of  
309 mesoscale eddies also induces the intense variability noted near the BMC. The high speed and deviation are constraints in an  
310 area where the retroflection of the MC propagates eddies to the west. This region is known for the shelf-break upwelling,  
311 where the significant depth gradient and the proximity to the MC contribute to the enhanced mixing and upwelling (Figure  
312 1).

313



314

315 **Figure 6: Mean sea surface currents (m/s) (a) and standard deviation of the mean speed (m/s) for the NBC (b) and the BMC (c)**  
 316 **regions. The standard deviation considers the monthly variability of speed in the domain. The main BC and MC path appears with**  
 317 **currents speed above 0.3 m/s and 0.6 m/s, respectively, while the speed of the NBC is above 1 m/s.**

318

319 The presence of eddies relates to the transference from mean potential to mean kinetic energy, observed by the Sea Surface  
 320 Height (SSH) variability and MKE in Figure 7. The MKE pattern displays the highest values where the highest speed is  
 321 placed, as expected for both WBCs, but the variability in the SSH is observed only in the BMC (Figure 7d). The  
 322 high-resolution benefits the maintenance of the MKE distribution, particularly in the BMC, where the eddies are the major  
 323 variability driver. To the west of  $55^{\circ}W$ , the Patagonian Shelf circulation is guided by the interaction of semidiurnal and

324 diurnal tidal components with the bottom friction and wind stress (Palma et al., 2004, 2008). The speed of the currents in the  
325 southern Patagonian Shelf in the model output represents this dynamical effect (Figure 6a). In other parts of the domain, the  
326 variability in the SSH is higher only in the river mouth. This indicates the influence of barotropic tides, which intensely  
327 modify the SSH in shallower regions. The MKE distribution and intensity of  $> 0.2 \text{ m}^2/\text{s}^2$  are similar to observations (Oliveira  
328 et al., 2009), and the distribution agrees with reanalysis (Poli et al., 2022). The high variability in the BMC occurs due to the  
329 physical processes related to the confluence of the BC and MC, which, near the Patagonian shelf, promote eddy formation  
330 due to the continental slope. As it shows fewer SSH deviations, the propagation of eddies in the NBC in this simulation is  
331 reduced. This suggests that the energy cascade primary process may not only drive eddy formation in this region but also  
332 other physical dissipative processes. The distinguished aspects found for the NBC and the BMC are covered in different  
333 sections in the following chapter, where this study evaluated the seasonal variability and trends.

#### 334 **4. Seasonal Variability and Trends of the WBCs**

##### 335 **4.1 Brazil-Malvinas Confluence**

336 The high variability in the BMC occurs due to the physical processes related to the confluence of the BC and MC, which,  
337 near the Patagonian shelf, promote eddy formation due to the continental slope (Oliveira et al., 2009). Mesoscale variability  
338 and eddy propagation are often diagnosed from the SSH standard deviation (Figure 6). The model patterns show consistency  
339 with those analyzed by Oliveira et al. (2009), using observed data from drifting buoys interpolated onto a  $0.5^\circ \times 0.5^\circ$  grid. The  
340 model also shows similarity with the observed MKE field from other studies (Oliveira et al., 2009, Combes and Matano,  
341 2014a) (Figure 7). Several authors have emphasized the importance of wind stress in maintaining the barotropic component  
342 of the circulation of the northern Patagonian Shelf (Lago et al., 2019; Campos et al., 2013; Palma et al., 2008, 2004; Combes  
343 and Matano, 2018). The most prominent influence is during the well-mixed period (JJAS) rather than in the stratified period  
344 (JFMA), when the baroclinic component is more relevant (Lago et al., 2019). This effect can be diagnosed in the  
345 climatological field in Figure 7. The presence of eddies in the annual average enhances the standard deviation of SSH and  
346 reveals the baroclinic component. The barotropic component is related to the total MKE distribution in the annual average in  
347 Figure 7c. It is confirmed that the main variability of the velocity fields is related to eddy propagation, which drives the SSH  
348 variability. The model consistently preserves the circulation features of the BMC even in regions close to shallow shelves.

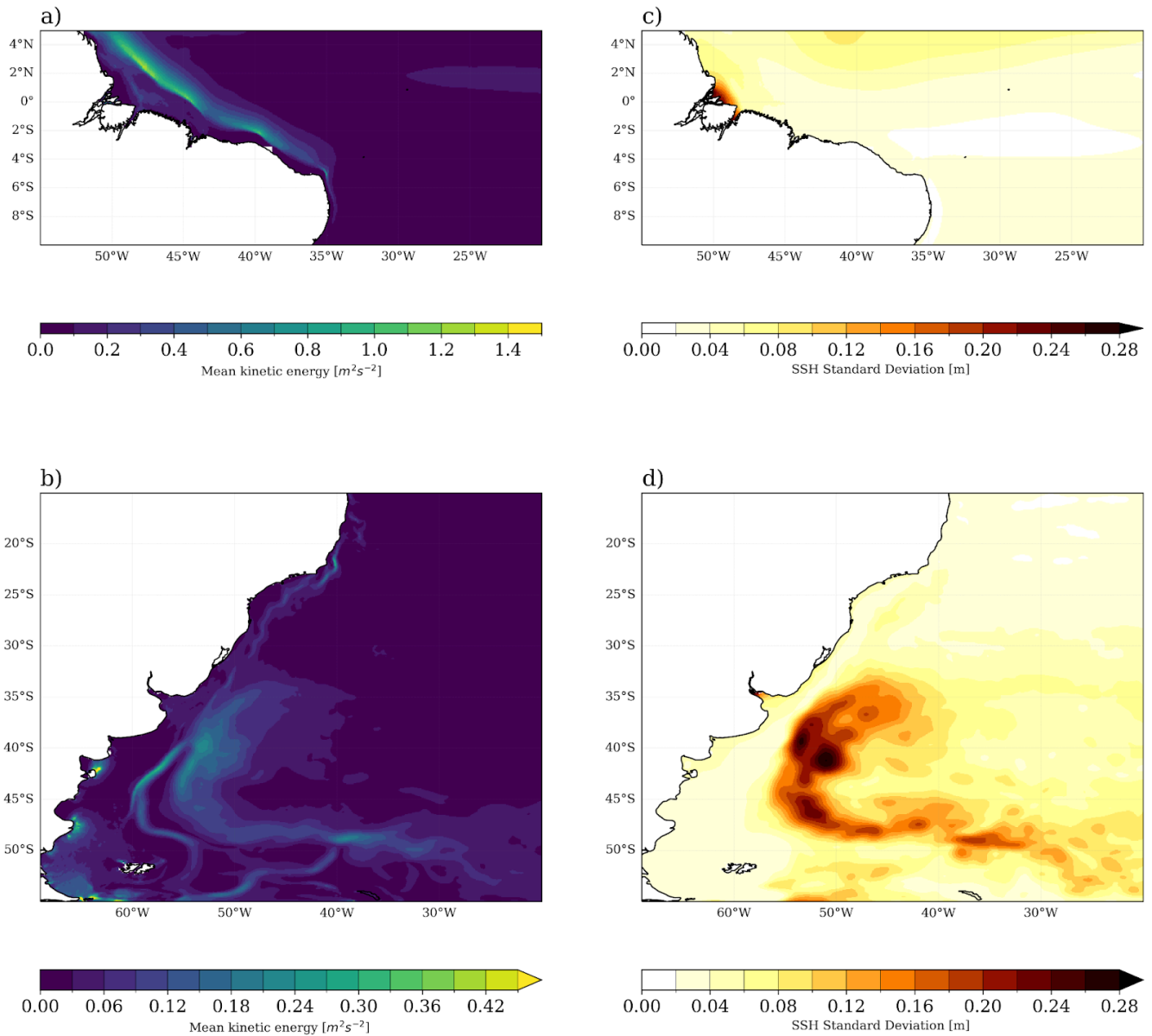
349

350 The model captures the seasonal behavior of the BC and the MC, revealing the density variations through the seasons in  
351 Figure 3. This implies that the MC takes a northern place during the colder seasons in this hemisphere (JJA, SON) while the  
352 BC advances during the warmer seasons (DJF, MAM). This is also evident in the seasonal cycle of the BC and MC transport  
353 (Figure 8) and in the number of extremes per season (Figure 10). The model registered below-average transport for the MC  
354 from October through April and above-average transport from May through September. The BC has the opposite cycle, and  
355 above-average southward transport occurs from December until April. The seasonal cycle is similar to what was found by

356 Combes and Matano (2014b) with ROMS simulations. Despite this, ROMS presents a higher MC mean transport of around  
357 73.1 Sv at 41°S compared to MOM6's 60.3 Sv transport at 45°S (Figure 8). The BC transport is higher in this simulation,  
358 around 57.9 Sv, while ROMS registers 40 Sv at 33°S.

359

360 The transport of the BC and MC shows a high interannual variability, as depicted in Figure 8. They can widely vary their  
361 transport from 10 to 88 Sv, with smaller transport in the BC (Goni et al., 2011). The increased MC transport induces the  
362 seasonal negative temperature bias in the 20-year mean temperature patterns from MAM until SON (Figure 3). Besides, the  
363 transports show a negative trend, more than 10 times higher than the trend obtained with observations (Goni et al., 2011).  
364 This could imply a systematic error in the simulation. Studies indicated that adjustments in the model bottom friction modify  
365 the mean northern ACC transport, inducing changes in the mean BMC (Combes and Matano, 2014a; Peterson, 1992;  
366 Combes and Matano, 2014b). As in this simulation, the ACC transport is given through reanalysis data, the bottom friction is  
367 the parameter that could interfere with the MC variability. However, the BC offers a balanced higher southward trend, which  
368 other studies have indicated as a consequence of Atlantic Ocean warming (Lumpkin and Garzoli, 2011; Risaro et al., 2020).



369

370 **Figure 7: Standard deviations of the Mean Kinetic Energy ( $m^2s^{-2}$ ) (a,b) and SSH (m) (c,d) in the regions of the WBCs. In the latter,**  
 371 **fields are std concerning the monthly variability from 1997 until 2017.**

372

373 Although the BMC separation occurs on average between the latitudes 37°S and 39°S (Goni et al., 2011), several studies  
 374 have recorded climatic trends of a southward shift in the BMC position. The trend is induced by the intense warming  
 375 observed in this ocean (Risaro et al., 2022; Franco et al., 2020), but the intensity of this relation and variability is still  
 376 uncertain. According to Goni et al. (2011), with satellite observations, this trend has a rate of 1.5° per decade between

377 1993-2008. Lumpkin and Garzoli (2011) indicated a varying rate between 0.6 to 0.9° per decade with data from 1992 until  
378 2007. A numerical model used by Combes and Matano (2014b) revealed a displacement of 0.62° per decade, which the  
379 study related to the weakening of the ACC.

380

381 The BMC separation obtained from model outputs is the latitude where the 1000 m isobath meets the 10°C isotherm at 200  
382 m, which, according to Garzoli and Bianchi (1987), depicts a location of enhanced time-space variability of the front  
383 separation. For the 20-year MOM6 simulation, the mean BMC separation is at  $36.76^{\circ}\text{S} \pm 0.77^{\circ}$ , as depicted in Figure 2. The  
384 plot shows the mean position obtained with GLORYS12v1 for the same period and by Goni et al. (2011), which considered  
385 satellite observations from 1993 until 2008. The model simulation is slightly ( $\approx 1^{\circ}$ ) more northerly than the other estimates  
386 in the plot. Using ROMS, Combes and Matano (2014b) estimate that the BMC separation is  $\approx 2^{\circ}$  farther south, around  $39^{\circ}\text{S}$ .  
387 The same reanalysis from GLORYS12v1 has been used in other studies have depicted a similar BMC separation near  $38^{\circ}\text{S}$   
388 (Artana et al., 2019; 2021).

389

390 The 20-year simulation outputs allow for the characterization of trends in this ocean, which is important for diagnosing the  
391 variability of the mean state. The model overestimated the BMC separation trend over the years compared to observations.  
392 The simulation registers a  $-0.93^{\circ}/\text{decade}$  deviation, while Goni et al. (2011) obtained different results based on observations  
393 of SST and SSH, with values of  $-0.39^{\circ}$  and  $-0.81^{\circ}$  per decade, respectively. Lumpkin and Garzoli (2011) indicate a trend  
394 between 0.6 and  $0.9^{\circ}/\text{decade}$  for 1992-2007. Despite the higher trend, the model mean BMC separation is close to other  
395 estimates (Figure 2), indicating that the model seasonal bias is compensated and the MC positioning is stable in this  
396 simulation.

397

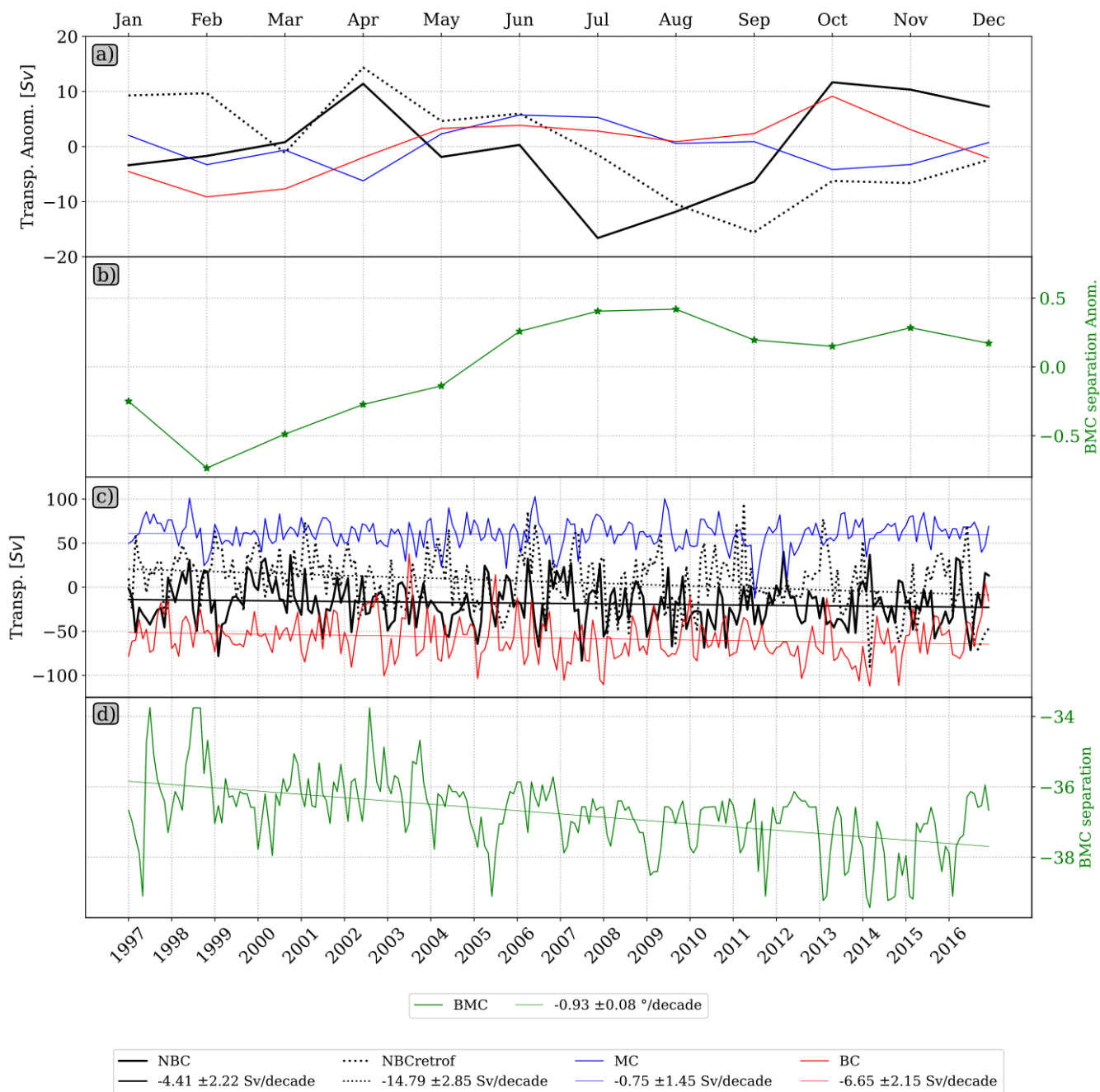
398 The trends of surface variables in Figure 9 depict important patterns in the BMC region. The temperature in the BMC is very  
399 similar to the pattern obtained with satellite observations for the 1982–2017 period (Risaro et al., 2020). The temperature is  
400 warmer in most BMC vicinities, while it is cooler in the southern part of the domain, representing more than 0.5 std.  
401 Enhancing the polar northward flow from the Drake Passage contributes to the negative SST and SSS trend, resulting in  
402 fresher and colder waters. In the BMC region, surface speed trends present a similar pattern; accordingly, warmer and saltier  
403 waters are faster and have increased transport, while colder and fresher waters are slower. This agrees with the number of  
404 BMC separation location extremes in Figure 10, which reduces significantly through the years, confirming the southward  
405 movement. In a warmer environment, the transport generated by the BMC presents stronger initial energy, but its track has a  
406 southward displacement.

407

408 Concerning the patterns far from the coast, there is a warming longitudinal trend pattern at  $35^{\circ}\text{S}$  extending from  $35^{\circ}\text{W}$  until  
409  $15^{\circ}\text{W}$ , evident in the model but not in the observations (Risaro et al., 2020). The region is known for its constant westward

410 flow and propagation of eddy from the Agulhas Current (Guerra et al., 2018). This indicates an intensification of the  
 411 transport to the north of 35°S in comparison to what is observed farther south.

412



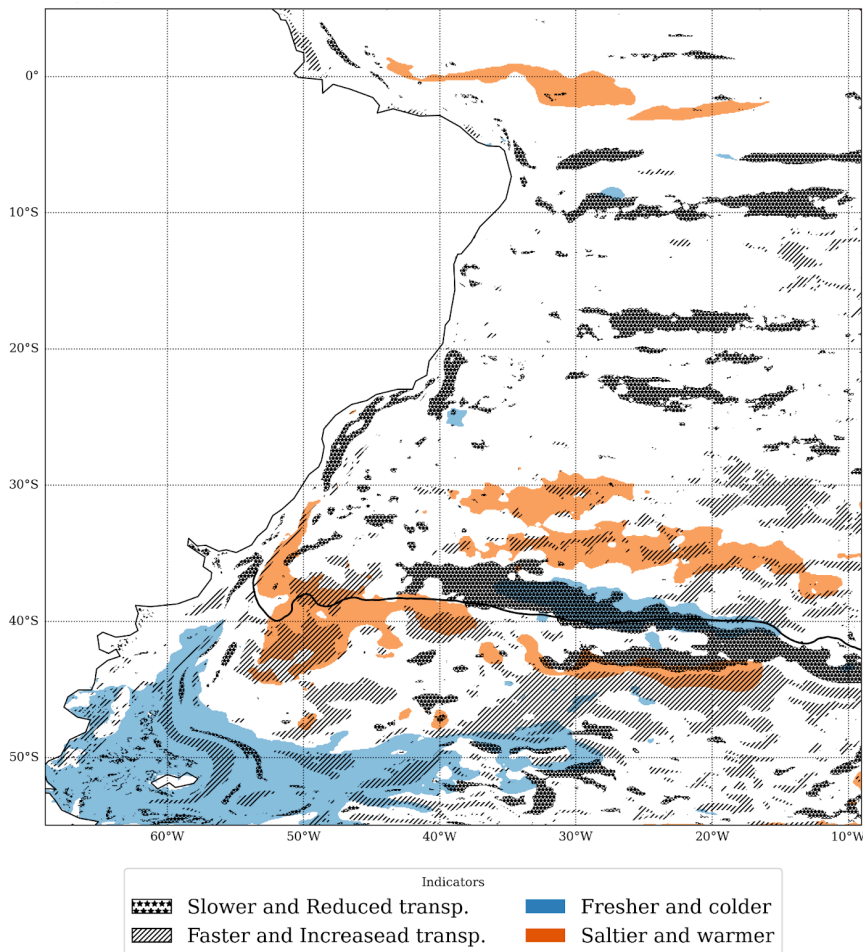
416 anomalies. The third row depicts the interannual transport for the WBC, and the bottom row shows the BMC positioning. The  
417 ocean transport is vertically integrated between latitudes  $0^{\circ}$  and  $3.5^{\circ}\text{N}$  for the NBC and  $4^{\circ}$  and  $5^{\circ}\text{N}$  for its retroflexion, whereas it  
418 is at latitudes  $45^{\circ}\text{S}$  and  $33^{\circ}\text{S}$  for the MC and BC, respectively. The transects are depicted in Figure 2. The positive transport flows  
419 northward and east, and the negative transport flows south and west.

#### 420 4.2 North Brazil Current

421 The NBC presents high variability associated with the propagation of eddies (Bueno et al., 2022; Garzoli et al., 2004). The  
422 model, however, underestimates the SSH variability in the NBC retroflexion, which suggests there is weaker transport from  
423 the SEC to the NBC. Some authors use zonal transport estimates based on NBC propagation and retroflexion sections to  
424 verify this diagnosis (Garzoli et al., 2004). The region is marked by intense currents, registering transport of  $16 \pm 2$  Sv for  
425 the NBC and  $22 \pm 2$  Sv for the retroflexion obtained by Garzoli et al. (2004). Accordingly, the estimates for the same  
426 sections with MOM6 outputs indicate that the 20-year average transport is around 18.4 Sv for the NBC. For its retroflexion,  
427 however, the transport series initiated with an amount of 22 Sv but indicated an average of 5.9 Sv. Garzoli et al. (2004)  
428 considered a 15-month mean by local sounders measurements, registering a seasonal cycle with more intense transport  
429 during ASO, less intense during MAM for the NBC, and the opposite for its retroflexion. The MOM6 simulation fails to  
430 reproduce any of these characteristics for the retroflexion (Figure 8a).

431

432 With a maximum latitude at  $5^{\circ}\text{N}$ , the simulation in this domain cannot fully develop the NBC retroflexion and its eddies as  
433 its natural path can deviate from  $4^{\circ}\text{N}$  to  $8^{\circ}\text{N}$  (Bueno et al., 2022; Valerio et al., 2021). The negative trend of the NBC  
434 retroflexion reveals that NBC reduced its transport in the model, but it also indicates that its path has deviated over the years  
435 and moved outside the model's domain. Despite that, features like temperature, salinity, and transport of the currents in the  
436 NBC and tropical region are precisely described during MAM. The bias appearing during JJA is maintained through the  
437 colder seasons (Figure 3). This indicates a lack of mixing, which can be either due to the influence of the wind speed (Figure  
438 5c) or the use of a z-coordinate vertical structure (Figure 5b). Interactions of the winds and the currents are important for  
439 mixing and eddy kinetic energy supply (Song et al., 2020). Thus, insufficient winds could reduce eddy formation, reducing  
440 the seasonal NBC retroflexion transport.



441

442 **Figure 9: Trends in the WBCs. Trends of different surface variables simulated by the model. Trends originate from a 36-month**  
 443 **running mean smothered series of standardized anomalies (Risaro et al., 2020). Colored regions are significant at a 95%**  
 444 **confidence level, according to Mann-Kendall's test. The trends by decade are normalized, and the colors display anomalous**  
 445 **patterns above 0.5 std.**

446

447 Although this simulation cannot fully represent the development of the NBC retroflection, investigating this deviation is  
 448 crucial to determine the variability of some climate patterns in the equatorial region, such as the storm track, the AMOC, and  
 449 the ITCZ. The absence of eddy propagation (Figure 7) and transport (Figure 8) in the region, for instance, might indicate  
 450 deviation in the dynamical structure of the model. Nevertheless, the model conserves large-scale SEC transport since the  
 451 mean NBC eastward transport resembles values slightly closer than those obtained from local measurements (Garzoli et al.,  
 452 2004). Still, many other factors could disfavor the propagation of NBC eddies. The proximity to the northern boundary is a  
 453 critical limiting factor, since this front could change its position through the years. However, it is also important to indicate  
 454 that the negative trend observed in the region can be related to atmospheric mechanisms and trends.

455

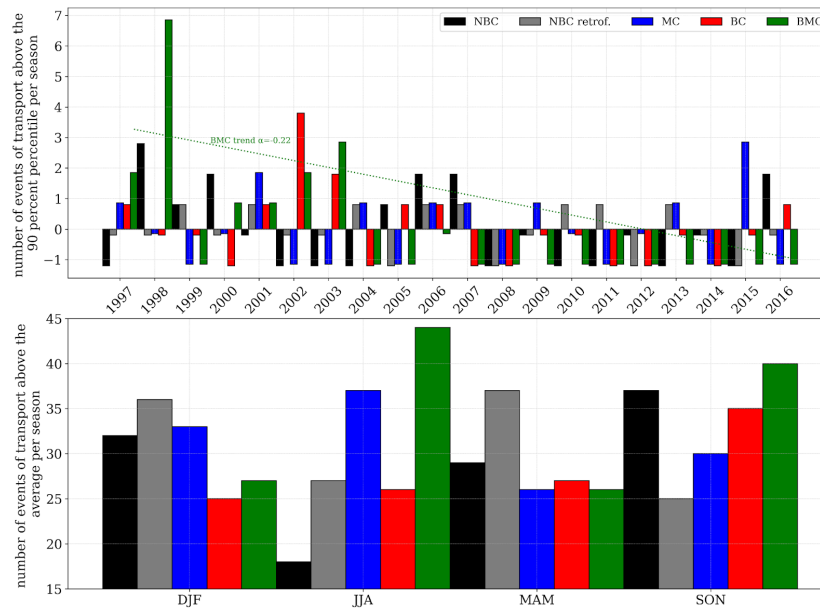
456 The trends in Tropical Atlantic Ocean waters indicate elevated temperature and salinity, as shown in Figure 9. This trend is  
457 not associated with transport and speed patterns. The Amazon River flow increases the transport and current speed in the  
458 northwestern part of the domain. The merged patterns of current speed and transport attenuate the eccentricity of the currents  
459 in the region, as revealed in Figure 8b. Thus, while the NBC and its retroflection experience a reduction in transport, they  
460 exhibit an increase in speed. The lack of stratification, as shown in Figure 4, suggests an inefficient transport of momentum  
461 to the sub-surface layers. This may also be influenced by external forcings or the redistribution of flow pathways out of the  
462 domain.

### 463 **4.3 Evaluation of external and internal forcings**

464 The WBCs in the Southwestern Atlantic domain feature intense variability and trends. This has been indicated by trends in  
465 the mean state of the surface variables (Figure 9), along with a tendency toward reduced extreme transport (Figure 10).  
466 Furthermore, extreme transports in the BC/MC are associated with the displacement of the BMC. In 1998, a year of an  
467 elevated number of extreme BMC displacements, the signal that enhances the southward movement of the BMC is unrelated  
468 to the transport amount toward the region. Thus, external teleconnections also generate modulations of the currents in the  
469 region. This section further investigates the components of this modulation.

470

471 External forcing, such as atmospheric teleconnections, can explain the mixed signals of the trend, indicating that the  
472 influence is not driven strictly by local forcings. Combes and Matano (2018) observed that the La Plata Basin flows are  
473 linked to the interannual variability of the ENSO. The correlation coefficients between the WBCs and climate indices  
474 indicate the susceptibility of the MC to Eastern Pacific Ocean variability, with significant correlation between its transport  
475 and the Nino1.2 and the PDO indices of 0.14 and 0.18, respectively. The BMC also presents a significant correlation of 0.26  
476 with the Nino1.2 index. These relations combine tropical and extratropical teleconnections with atmospheric components  
477 that drive turbulence and freshwater discharge in the domain (Combes and Matano, 2018), resulting in strong MC and  
478 northern BMC in response to rising temperatures in the Eastern Pacific.



479

480 **Figure 10: Registries of extreme transport events in the WBCs. The graphics show the events from 1997 to 2016 with transport**  
 481 **above the 90 percent percentile per year (top) and above the average per season (bottom).**

482

483 Due to the proximity to the coastal slopes, the internal variability of the currents and transport in the WBCs results in a  
 484 broader number of dynamic interactions, different from those in the open ocean (Hughes et al., 2019). The wave propagation  
 485 from tropical regions in the Pacific follows the western South American coastline, which propagates and contributes to the  
 486 coastal dynamics in the Southwest Atlantic Ocean. Poli et al. (2022) reveal that Kelvin wave dispersion and Rossby wave  
 487 propagation from the Madden-Julian Oscillation are linked to the barotropic and baroclinic components of the coastal  
 488 trapped waves in the Southwest Atlantic Ocean.

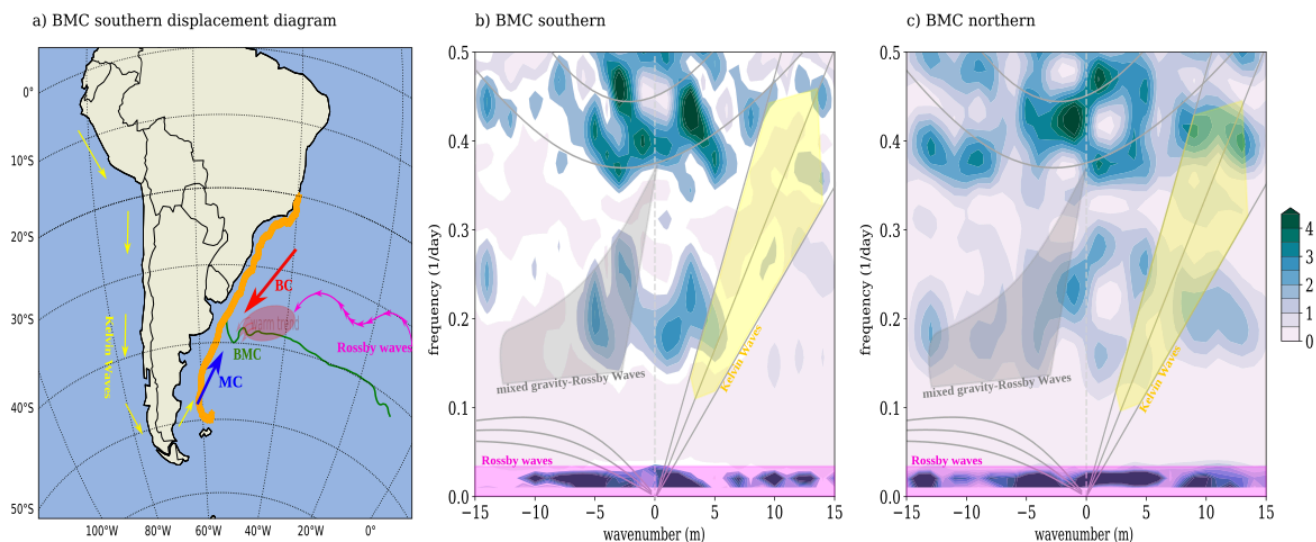
489

490 To examine the waves occurring on the coastline in the model outputs, we plot a dispersion diagram following Wheeler and  
 491 Kiladis (1998). The diagram reveals the spectrum eccentricity of a determined location at a determined period in time,  
 492 enabling the dynamic patterns to be classified by frequency and wavenumbers. Figure 11 displays the distinctive patterns  
 493 during two distinct behaviors of the BMC separation: southern and northern extreme shifts. The wave patterns indicate that  
 494 this region is influenced by coastal and open ocean dynamics. In the diagram, the low-frequency energy waves of positive  
 495 and negative wavenumbers reveal the influence of eastward and westward Rossby wave propagation. This region is affected  
 496 by westward waves that could be driven by MJO propagation (Poli et al., 2022), while the eastward waves are a response to  
 497 the Indian Ocean Rossby Wave propagation from the Agulhas Current (Pontes and Menviel, 2022). Another important  
 498 pattern is the higher-frequency modes, whose behavior is similar to that of inertial gravity waves, and its associate this  
 499 pattern with the coastal trapped wave disturbance. Despite the high frequency, the inertial gravity waves in this region have

500 shorter wavelengths. Their propagation is constrained in the region and is mainly interacting with the bottom topography,  
 501 and with other wave patterns (Alford et al., 2016). The driver is sustained by local variations in density and temperature on  
 502 the ocean surface due to wind forcing. The most important aspect of this pattern in the region is the interaction of inertial  
 503 gravity waves with the mesoscale and submesoscale motions (Alford et al., 2016).

504

505 Different energy spectra occur during the distinct events for mid-frequency waves, classified as mixed gravity-Rossby Waves  
 506 and Kelvin Waves (Figure 11, marked in grey and yellow). The propagation of Kelvin Waves also relates to external forcing  
 507 from equatorial sources (Hughes et al., 2019; Poli et al., 2022). According to Poli et al. (2022), the MJO propagation trigger  
 508 Kelvin Waves propagation in Central Pacific that reaches the South Atlantic driving coastal trapped waves into the  
 509 Southwest Atlantic Ocean. This results in strong trigger for waves propagating northward (Poli et al., 2022), auxiliating the  
 510 acceleration of the northern MC and northern BMC. The diagram confirms that coastal trapped waves energetic disturbance  
 511 contributes to northern BMC displacement, which is presented here in response to rising temperatures in the Eastern Pacific.  
 512 This result increases the understanding of the drivers of extreme shifts in the BMC separation.



513

514 **Figure 11: Diagram with the interactions in the BMC region modifying its displacement (a). Frequency and wavenumber diagram**  
 515 **during extreme meridional displacement of the BMC separation: b) BMC southern in 2014, c) BMC northern in 1997. The**  
 516 **spectrum reveals the frequency and wavenumber in the model SSH outputs band-pass series filtered between 40 and 130 days for**  
 517 **the 300 m isobath between latitudes 20°S and 50°S. The diagram is for the transect along the 300m isobath, in orange.**

518

## 519 5. Summary and Conclusions

520 This work analyzed the representation of the Southwestern Atlantic circulation using a 20-year MOM6 simulation at a 7 km  
521 resolution, focusing on the variability of the WBCs. The results first explore the performance of the simulation, which has  
522 proven to be skillful when compared to observational and reanalysis datasets. The Eddy-permitting resolution allows a better  
523 representation of the SST and SSS fields than coarser resolution simulations. The model accurately captured surface ocean  
524 circulation and temperature and salinity gradients. The maximum negative SST bias of 1.0°C is sufficiently good  
525 performance for forecasting ocean conditions. The correspondence between density and MLD to the salinity and temperature  
526 structure indicates that the model reproduces thermodynamic effects fairly. Their effects on the density field drive the  
527 large-scale circulation, as highlighted by the global circulation and mesoscale features.

528

529 The transport of the currents in the simulation has evolved over decades in the Southwestern Atlantic WBCs. The BMC  
530 separation is a region with stronger kinetic energy in the domain. Observing the components of the BMC variability can help  
531 identify the location of eddy propagation and shelfbreak upwelling. Although it has been related to the bottom drag, the  
532 enhanced southward shift in the BMC is also consistent with the heating trend in this study. The warming Atlantic is  
533 followed by a modified BC transport with an increase of  $6.65 \pm 2.15$  Sv in the southward flow per decade. This feature is  
534 usually balanced by the conservation of the MC transport. The trends show enhanced northward transport of fresher and  
535 colder waters from the ACC, which reduces the temperature by bringing cool waters to the region. Despite this, the trends  
536 modify the location of the BMC separation, with a southward displacement of  $0.93 \pm 0.08$  °/decade.

537

538 We show that the location of the BMC separation has extremes that relate to natural climate variability patterns in the Pacific  
539 Ocean. The Pacific Ocean warming has a stronger correlation and enhanced activity during MC transport extremes and  
540 northward BMC. The Nino1.2 (East Niño) and PDO indices corroborate this behavior. The impacts are explained by a  
541 spectral analysis, which reveals Rossby and Kelvin Wave-like disturbances, in addition to the inertial gravity waves intrinsic  
542 in the slope proximity. Eastward and westward propagating Rossby waves occur as a link between tropical disturbances  
543 such as the MJO and the Agulhas Current (Guerra et al., 2018; Poli et al., 2022). The Kelvin wave disturbances appear to be  
544 the main energy source for the BMC separation latitudinal shift, revealing strong spectral power for a northern BMC  
545 positioning as they propagate northward. This indicates that although the warmer Atlantic enhances the southward shift in  
546 the BMC separation, mechanisms intensified by the warmer Eastern Pacific can enhance the northward flow.

547

548 The NBC also presents reduced transport, but the model has captured a higher negative trend than that of the one in the BC.  
549 The unbalanced reduction of  $14.79 \pm 2.85$  Sv per decade for its retroflexion weakly correlates with natural climate  
550 variability patterns. Still, other contributing factors can explain the intense influences observed in the NBC activity. We  
551 found that the transport trends occur alongside a positive current speed trend. Since much of the variability of the ocean

552 surface currents receives a direct contribution from the wind, weaker winds lead to reduced NBC eastward propagation with  
553 fewer eddies. Along with the absence of winds, we show a reduced stratification pattern commonly linked to lower  
554 temperatures and, consequently, the transport in adjacent layers. Additionally, the reduced transport registered by the model  
555 in the tropical regions could be associated with the proximity to the northern boundaries and the modification of flow  
556 pathways, which should be addressed in future research.

557

558 The coordinate system is also relevant to the deviated stratification structure captured by the model in the equatorial region.  
559 Studies have indicated that the reduced mixing in the ocean interior is inherent to vertical z-coordinate system models,  
560 especially in highly stratified regions (Adcroft et al., 2019; Griffies et al., 2000). This could contribute to the bias found in  
561 the equatorial and Amazonian regions but also can lead to the lack of mixing in the La Plata basin outflow region.

562

563 The analysis of the model output has proven helpful in diagnosing how the WBC dynamics are expected to vary under a  
564 changing climate. We suggest that future experiments evaluate the efficiency of other coordinate systems in this domain. The  
565 displacement of such energetic regions can cause tremendous impacts on marine ecosystems. We advise future research to  
566 integrate a biogeochemistry model to diagnose this interaction specifically. Furthermore, an analysis comprising the  
567 atmospheric feedback under the displaced WBCs is also recommended, as the Southwestern Atlantic Ocean presents an  
568 important relationship with atmospheric systems (Laureanti et al., 2024).

569

570

571 *Code and Data Availability.* The datasets used for model validation and comparison are listed as follows: mixed-layer depth  
572 ([https://mld.ifremer.fr/Surface\\_Mixed\\_Layer\\_Depth.php](https://mld.ifremer.fr/Surface_Mixed_Layer_Depth.php), De Boyer Montéut et al., 2004), QSCAT wind speed  
573 (<https://podaac.jpl.nasa.gov/QuikSCAT?tab=-mission-objectives&sections=about%2Bdata>, Hoffman and Leidner, 2005),  
574 PIRATA (<https://www.pmel.noaa.gov/gtmba/pmel-theme/atlantic-ocean-pirata>, Servain et al., 1998) and World Ocean Atlas  
575 2023 (<https://www.ncei.noaa.gov/access/metadata/landing-page/bin/iso?id=gov.noaa.nodc:NCEI-WOA23>, Reagan et al.,  
576 2023).

577

578 The datasets used to create the model forcing are listed as follows: GLORYS12v1 reanalysis  
579 (<https://doi.org/10.48670/moi-00021>, Global Ocean Physics Reanalysis, 2021), TPXO9 (<https://www.tpxo.net/home>, Egbert  
580 and Erofeeva, 2002), GloFAS (<https://doi.org/10.24381/cds.a4fdd6b9>, Zsoter, 2019), GEBCO (<https://download.gebco.net/>,  
581 Giribabu et al., 2023) SeaWIFS (<https://oceandata.sci.gsfc.nasa.gov/>, NASA, 2018) and ERA5  
582 (<https://cds.climate.copernicus.eu/datasets>, Hersbach et al., 2023). The model source code is uploaded in  
583 <https://zenodo.org/records/17252994> and scripts for setting-up are in <https://zenodo.org/records/17252554>. The model  
584 outputs are available under the link  
585 <http://antares.esm.rutgers.edu:8080/thredds/catalog/MOM6/ESMG/SWA14/exp.010/catalog.html>

586

587 *Author contributions.* The authors contributed equally to this work.

588

589 *Competing interests.* The authors declare no conflict of interest.

590

591 *Acknowledgements.* The authors thank the Coordenação de Aperfeiçoamento de Pessoal de Nível Superior (CAPES) Finance  
592 Code 001 for its financial support and the Earth System Modelling Laboratory at Rutgers University.

593 Part of this work used resources from the Centro Nacional de Processamento de Alto Desempenho em São Paulo  
594 (CENAPAD-SP) in Brazil and also the high-performance computing support from Cheyenne (doi:10.5065/D6RX99HX)  
595 provided by NCAR's Computational and Information Systems Laboratory, sponsored by the National Science Foundation.  
596 SCC thanks CNPq for the grant no. 312742/2021-5.

## 597 6. References

598 Adcroft, A. and Campin, J.-M.: Rescaled height coordinates for accurate representation of free-surface flows in ocean  
599 circulation models, *Ocean Modelling*, 7, 269–284, <https://doi.org/10.1016/j.ocemod.2003.09.003>, 2004.

600 Adcroft, A., Anderson, W., Balaji, V., Blanton, C., Bushuk, M., Dufour, C. O., Dunne, J. P., Griffies, S. M., Hallberg, R.,  
601 Harrison, M. J., Held, I. M., Jansen, M. F., John, J. G., Krasting, J. P., Langenhorst, A. R., Legg, S., Liang, Z., McHugh, C.,  
602 Radhakrishnan, A., Reichl, B. G., Rosati, T., Samuels, B. L., Shao, A., Stouffer, R., Winton, M., Wittenberg, A. T., Xiang,  
603 B., Zadeh, N., and Zhang, R.: The GFDL Global Ocean and Sea Ice Model OM4.0: Model Description and Simulation  
604 Features, *Journal of Advances in Modeling Earth Systems*, 11, 3167–3211, <https://doi.org/10.1029/2019MS001726>, 2019.

605 Aiki, H., Zhai, X., and Greatbatch, R. J.: Energetics of the global ocean the role of mesoscale eddies, chap. 4, pp. 109–134,  
606 [https://doi.org/10.1142/9789814696623\\_0004](https://doi.org/10.1142/9789814696623_0004), 2015.

607 Alford, M. H., MacKinnon, J. A., Simmons, H. L., and Nash, J. D.: Near-Inertial Internal Gravity Waves in the Ocean.  
608 *Annual review of marine science*, 8, 95-123, 2016.

609 Artana, C., & Provost, C.: Intense anticyclones at the global Argentine Basin array of the Ocean Observatory Initiative.  
610 *Ocean Science*, 19(3), 953–971. <https://doi.org/10.5194/OS-19-953-2023>, 2023.

611 Artana, C., Provost, C., Poli, L., Ferrari, R. & Lellouche, J.-M.: Revisiting the Malvinas Current upper circulation and water  
612 masses using a highresolution ocean reanalysis. *Journal of Geophysical Research: Oceans*, 126(6),  
613 [doi.org/10.1029/2021JC017271](https://doi.org/10.1029/2021JC017271), 2021.

614 Artana, C., Provost, C., Lellouche, J.-M., Rio, M.-H., Ferrari, R., & Sennéchaël, N.: The Malvinas Current at the Confluence  
615 with the Brazil Current: Inferences from 25 years of Mercator Ocean reanalysis. *Journal of Geophysical Research: Oceans*,  
616 124, 7178–7200, <https://doi.org/10.1029/2019JC015289>, 2019.

617 Barré, N., Provost, C., & Saraceno, M.: Spatial and temporal scales of the Brazil–Malvinas Current confluence documented  
618 by simultaneous MODIS Aqua 1.1-km resolution SST and color images. *Advances in Space Research*, 37(4), 770–786.  
619 <https://doi.org/10.1016/J.ASR.2005.09.026>, 2006

620 Bonou, F. K., Noriega, C., Lefèvre, N., & Araujo, M.: Distribution of CO<sup>2</sup> parameters in the Western Tropical Atlantic  
621 Ocean. *Dynamics of Atmospheres and Oceans*, 73, 47–60. <https://doi.org/10.1016/J.DYNATMOCE.2015.12.001>, 2016.

622 Brum, A. L., de Azevedo, J. L. L., de Oliveira, L. R., and Calil, P. H. R.: Energetics of the Brazil Current in the Rio Grande  
623 Cone region, *Deep Sea Research Part I: Oceanographic Research Papers*, 128, 67–81,  
624 <https://doi.org/10.1016/J.DSR.2017.08.014>, 2017.

625 Bueno, L. F., Costa, V. S., Mill, G. N., and Paiva, A. M.: Volume and Heat Transports by North Brazil Current Rings,  
626 *Frontiers in Marine Science*, 9, <https://doi.org/10.3389/fmars.2022.831098>, 2022.

627 Campos, P. C., Möller, O. O., Piola, A. R., and Palma, E. D.: Seasonal variability and coastal upwelling near Cape Santa  
628 Marta (Brazil), *Journal of Geophysical Research: Oceans*, 118, 1420–1433, <https://doi.org/10.1002/JGRC.20131>, 2013.

629 Chassignet, E. P. and Xu, X.: On the Importance of High-Resolution in Large-Scale Ocean Models,  
630 <https://doi.org/10.1007/s00376-021-0385-7>, 2021.

631 Combes, V. and Matano, R. P.: A two-way nested simulation of the oceanic circulation in the Southwestern Atlantic, *Journal*  
632 *of Geophysical Research: Oceans*, 119, 731–756, <https://doi.org/10.1002/2013JC009498>, 2014a.

633 Combes, V. and Matano, R. P.: Trends in the Brazil/Malvinas Confluence region, *Geophysical Research Letters*, 41,  
634 8971–8977, <https://doi.org/10.1002/2014GL062523>, 2014b.

635 Combes, V. and Matano, R. P.: The Patagonian shelf circulation: Drivers and variability, *Progress in Oceanography*, 167,  
636 24–43, <https://doi.org/10.1016/J.POCEAN.2018.07.003>, 2018.

637 de Boyer Montégut, C., Madec, G., Fischer, A. S., Lazar, A., and Iudicone, D.: Mixed layer depth over the global ocean: An  
638 examination of profile data and a profile-based climatology, *Journal of Geophysical Research: Oceans*, 109,  
639 <https://doi.org/10.1029/2004JC002378>, 2004.

640 Egbert, G. D. and Erofeeva, S. Y.: Efficient Inverse Modeling of Barotropic Ocean Tides, *Journal of Atmospheric and*  
641 *Oceanic Technology*, 19, 183 – 204,  
642 [https://doi.org/https://doi.org/10.1175/1520-0426\(2002\)019<0183:EIMOBO>2.0.CO;2](https://doi.org/https://doi.org/10.1175/1520-0426(2002)019<0183:EIMOBO>2.0.CO;2), 2002.

643 Ferrari, R., Artana, C., Saraceno, M., Piola, A. R., & Provost, C.: Satellite Altimetry and Current-Meter Velocities in the  
644 Malvinas Current at 41°S: Comparisons and Modes of Variations. *Journal of Geophysical Research: Oceans*, 122(12),  
645 9572–9590. <https://doi.org/10.1002/2017JC013340>, 2017.

646 Fox-Kemper, B., Danabasoglu, G., Ferrari, R., Griffies, S. M., Hallberg, R. W., Holland, M. M., Maltrud, M. E., Peacock, S.,  
647 and Samuels, B. L.: Parameterization of mixed layer eddies. III: Implementation and impact in global ocean climate  
648 simulations, *Ocean Modelling*, 39,61–78, <https://doi.org/10.1016/j.ocemod.2010.09.002>, modelling and Understanding the  
649 Ocean Mesoscale and Submesoscale, 2011.

650 Franco, B. C., Defeo, O., Piola, A. R., Barreiro, M., Yang, H., Ortega, L., Gianelli, I., Castello, J. P., Vera, C., Buratti, C.,  
651 Pájaro, M., Pezzi, L. P., and Möller, O. O.: Climate change impacts on the atmospheric circulation, ocean, and fisheries in  
652 the southwest South Atlantic Ocean: a review, *Climatic Change*, 162, 2359–2377,  
653 <https://doi.org/10.1007/S10584-020-02783-6>, 2020.

654 Garzoli, S. L. and Bianchi, A.: Time-space variability of the local dynamics of the Malvinas-Brazil confluence as revealed  
655 by inverted echosounders, *Journal of Geophysical Research: Oceans*, 92, 1914–1922,  
656 <https://doi.org/https://doi.org/10.1029/JC092iC02p01914>, 1987.

657 Garzoli, S. L. and Matano, R.: The South Atlantic and the Atlantic Meridional Overturning Circulation, *Deep Sea Research*  
658 Part II: Topical Studies in Oceanography, 58, 1837–1847, <https://doi.org/10.1016/j.dsr2.2010.10.063>, climate and the  
659 Atlantic Meridional Overturning Circulation, 2011.

660 Garzoli, S. L., Ffield, A., Johns, W. E., and Yao, Q.: North Brazil Current retroflexion and transports, *Journal of*  
661 *Geophysical Research: Oceans*, 109, <https://doi.org/10.1029/2003JC001775>, 2004.

662 Giribabu, D., Hari, R., Sharma, J., Ghosh, K., Padiyar, N., Sharma, A., Bera, A. K., and Srivastav, S. K.: Assessment of  
663 GEBCO 2023 Gridded Bathymetric Data in Shallow Waters Using the Seafloor from ICESat-2 Photons, Preprint to *Marine*  
664 *Geophysical Research*, 2023, <https://doi.org/10.21203/rs.3.rs-3020167/v1>, 2023.

665 Goni, G. J., Bringas, F., and DiNezio, P. N.: Observed low frequency variability of the Brazil Current front, *Journal of*  
666 *Geophysical Research: Oceans*, 116, <https://doi.org/10.1029/2011JC007198>, 2011.

667 Griffies, S. M., Böning, C., Bryan, F. O., Chassignet, E. P., Gerdes, R., Hasumi, H., Hirst, A., Treguier, A.-M., and Webb, D.:  
668 Developments in ocean climate modelling, *Ocean Modelling*, 2, 123–192,  
669 [https://doi.org/https://doi.org/10.1016/S1463-5003\(00\)00014-7](https://doi.org/https://doi.org/10.1016/S1463-5003(00)00014-7), 2000.

670 Griffies, S. M., Winton, M., Anderson, W. G., Benson, R., Delworth, T. L., Dufour, C. O., Dunne, J. P., Goddard, P.,  
671 Morrison, A. K., Rosati, A., Wittenberg, A. T., Yin, J., and Zhang, R.: Impacts on ocean heat from transient mesoscale  
672 eddies in a hierarchy of climate models, *Journal of Climate*, 28, 952–977, <https://doi.org/10.1175/JCLI-D-14-00353.1>,  
673 2015.

674 Guerra, L. A. A., Paiva, A. M., Chassignet, E. P.: On the translation of Agulhas rings to the western South Atlantic Ocean,  
675 *Deep-Sea Research Part I*, 139, 104–113, 2018.

676 Guerrero, R. A., Piola, A. R., Fenco, H., Matano, R. P., Combes, V., Chao, Y., James, C., Palma, E. D., Saraceno, M., and  
677 Strub, P. T.: The salinity signature of the cross-shelf exchanges in the Southwestern Atlantic Ocean: Satellite observations,  
678 *Journal of Geophysical Research: Oceans*, 119, 7794–7810, <https://doi.org/10.1002/2014JC010113>, 2014.

679 Hallberg, R.: Using a resolution function to regulate parameterizations of oceanic mesoscale eddy effects, *Ocean Modelling*,  
680 72, 92–103, <https://doi.org/10.1016/j.ocemod.2013.08.007>, 2013.

681 Hersbach, H., Bell, B., Berrisford, P., Biavati, G., Horányi, A., Muñoz Sabater, J., Nicolas, J., Peubey, C., Radu, R., Rozum,  
682 I., Schepers, D., Simmons, A., Soci, C., Dee, D., Thépaut, J.-N. (2023): ERA5 hourly data on single levels from 1940 to

683 present. Copernicus Climate Change Service (C3S) Climate Data Store (CDS), DOI: 10.24381/cds.adbb2d47 (Accessed on  
684 24-Jan-2025)

685 Hoffman, R. N. and Leidner, S. M.: An Introduction to the Near-Real-Time QuikSCAT Data, *Weather and Forecasting*, 20,  
686 476 – 493, <https://doi.org/https://doi.org/10.1175/WAF841.1>, 2005.

687 Hughes, C.W., Fukumori, I., Griffies, S.M., Huthnance, J.M., Minobe, S., Spence, P., Thompson, K.R., Wise, A.: Sea  
688 Level and the Role of Coastal Trapped Waves in Mediating the Influence of the Open Ocean on the Coast. *Surv. Geophys.*,  
689 40, 1467–1492, <https://doi.org/10.1007/s10712-019-09535-x>, 2019

690 Jackson, L., Hallberg, R., and Legg, S.: A Parameterization of Shear-Driven Turbulence for Ocean Climate Models, *Journal*  
691 *of Physical Oceanography*, 38, 1033 – 1053, <https://doi.org/https://doi.org/10.1175/2007JPO3779.1>, 2008.

692 Jean-Michel, L., Eric, G., Romain, B.-B., Gilles, G., Angélique, M., Marie, D., Clément, B., Mathieu, H., Olivier, L. G.,  
693 Charly, R., Tony, C., Charles-Emmanuel, T., Florent, G., Giovanni, R., Mounir, B., Yann, D., and Pierre-Yves, L. T.: The  
694 Copernicus Global 1/12° Oceanic and Sea Ice GLORYS12v1 Reanalysis, *Frontiers in Earth Science*, 9,  
695 <https://doi.org/10.3389/feart.2021.698876>, 2021.

696 Kang, D., Curchitser, E. N., and Rosati, A.: Seasonal Variability of the Gulf Stream Kinetic Energy, *Journal of Physical*  
697 *Oceanography*, 46, 1189 – 1207, <https://doi.org/https://doi.org/10.1175/JPO-D-15-0235.1>, 2016.

698 Kendall, M. G. *Rank Correlation Methods*, 4th edition, Charles Griffin, London, 1975.

699 Lago, L. S., Saraceno, M., Martos, P., Guerrero, R. A., Piola, A. R., Paniagua, G. F., Ferrari, R., Artana, C. I., and Provost,  
700 C.: On the Wind Contribution to the Variability of Ocean Currents Over Wide Continental Shelves: A Case Study on the  
701 Northern Argentine Continental Shelf, *Journal of Geophysical Research: Oceans*, 124, 7457–7472,  
702 <https://doi.org/10.1029/2019JC015105>, 2019.

703 Laureanti, N. C., Chou, S. C., Nobre, P., and Curchitser, E.: On the relationship between the South Atlantic Convergence  
704 Zone and sea surface temperature during Central-East Brazil extreme precipitation events, *Dynamics of Atmospheres and*  
705 *Oceans*, 105, 10.1016/j.dynatmoce.2023.101422, 2024.

706 Locarnini, R., Mishonov, A., Baranova, O., Boyer, T., Zweng, M., Garcia, H., Reagan, J., Seidov, D., Weathers, K., Paver,  
707 C., Smolyar, I., and Locarnini, R.: *World Ocean Atlas 2018, Volume 1: Temperature*, 2019.

708 Lumpkin, R. and Garzoli, S.: Interannual to decadal changes in the western South Atlantic’s surface circulation, *Journal of*  
709 *Geophysical Research: Oceans*, 116, <https://doi.org/10.1029/2010JC006285>, 2011.

710 Lumpkin, R. and Garzoli, S. L.: Near-surface circulation in the Tropical Atlantic Ocean, *Deep Sea Research Part I:*  
711 *Oceanographic Research Papers*, 52, 495–518, <https://doi.org/10.1016/J.DSR.2004.09.001>, 2005.

712 Mann, H. B. Non-parametric tests against trend, *Econometrica* 1945, 13, 163-171.

713 Marcello, F., Tonelli, M., Ferrero, B., and Wainer, I.: Projected Atlantic overturning slow-down is to be compensated by a  
714 strengthened South Atlantic subtropical gyre, *Communications Earth & Environment* 2023 4:1, 4, 1–15,  
715 <https://doi.org/10.1038/s43247-023-00750-4>, 2023.

716 Mason, E., Pascual, A., Gaube, P., Ruiz, S., Pelegrí, J. L., and Delepoule, A.: Subregional characterization of mesoscale  
717 eddies across the Brazil-Malvinas Confluence, *Journal of Geophysical Research: Oceans*, 122, 3329–3357,  
718 <https://doi.org/10.1002/2016JC012611>, 2017.

719 Müller, V. and Melnichenko, O.: Meridional Eddy Heat Transport Variability in the Surface Mixed Layer of the Atlantic  
720 Ocean, *Journal of Geophysical Research: Oceans*, 126, e2021JC017 789, <https://doi.org/10.1029/2021JC017789>, 2021.

721 NASA: Sea-viewing Wide Field-of-view Sensor (SeaWiFS) level-2 ocean color data,  
722 <https://doi.org/10.5067/ORBVIEW-2/SEAWIFS/L2/OC/2018>, NASA Ocean Biology Processing Group distributed active  
723 archive center, 2018.

724 NOAA, National Oceanic and Atmospheric Administration, Physical Sciences Laboratory (PSL). Climate Indices: Monthly  
725 Atmospheric and Ocean Time-Series. Available online: <https://psl.noaa.gov/data/climateindices/list/> (accessed on 15 May  
726 2024).

727 Nobre, P., Lemos, A. T., Giarolla, E., Camayo, R., Namikawa, L., Kampel, M., Rudorff, N., Bezerra, D. X., Lorenzetti, J.,  
728 and Gomes, J.: The 2019 northeast Brazil oil spill: scenarios, *Anais da Academia Brasileira de Ciências*, 94, e20210 391,  
729 <https://doi.org/10.1590/0001-3765202220210391>, 2022.

730 Oliveira, L. R., Piola, A. R., Mata, M. M., and Soares, I. D.: Brazil Current surface circulation and energetics observed from  
731 drifting buoys, *Journal of Geophysical Research: Oceans*, 114, 10 006, <https://doi.org/10.1029/2008JC004900>, 2009.

732 Palma, E. D., Matano, R. P., and Piola, A. R.: A numerical study of the Southwestern Atlantic Shelf circulation: Barotropic  
733 response to tidal and wind forcing, *Journal of Geophysical Research: Oceans*, 109, 8014,  
734 <https://doi.org/10.1029/2004JC002315>, 2004.

735 Palma, E. D., Matano, R. P., and Piola, A. R.: A numerical study of the Southwestern Atlantic Shelf circulation: Stratified  
736 ocean response to local and offshore forcing, *Journal of Geophysical Research: Oceans*, 113, 11 010,  
737 <https://doi.org/10.1029/2007JC004720>, 2008.

738 Peterson, R. G.: The boundary currents in the western Argentine Basin, *Deep Sea Research Part A. Oceanographic Research*  
739 *Papers*, 39, 623–644, [https://doi.org/https://doi.org/10.1016/0198-0149\(92\)90092-8](https://doi.org/https://doi.org/10.1016/0198-0149(92)90092-8), 1992.

740 Pezzi, L. P., Quadro, M. F., Lorenzetti, J. A., Miller, A. J., Rosa, E. B., Lima, L. N., and Sutil, U. A.: The effect of Oceanic  
741 South Atlantic Convergence Zone episodes on regional SST anomalies: the roles of heat fluxes and upper-ocean dynamics,  
742 *Climate Dynamics*, 59, 2041–2065, <https://doi.org/10.1007/S00382-022-06195-3/TABLES/1>, 2022.

743 Pilo, G. S., Mata, M. M., and Azevedo, J. L.: Eddy surface properties and propagation at Southern Hemisphere western  
744 boundary current systems, *Ocean Science*, 11, 629–641, <https://doi.org/10.5194/OS-11-629-2015>, 2015.

745 Piola, A. R., Matano, R. P., Palma, E. D., Möller, O. O., and Campos, E. J. D.: The influence of the Plata River discharge on  
746 the western South Atlantic shelf, *Geophysical Research Letters*, 32, 1–4, <https://doi.org/10.1029/2004GL021638>, 2005.

747 Poli, L., Artana, C., and Provost, C.: Topographically trapped waves around South America with periods between 40  
748 and 130 days in a global ocean reanalysis. *Journal of Geophysical Research: Oceans*, 127, e2021JC018067, [https://doi.](https://doi.org/10.1029/2021JC018067)  
749 [org/10.1029/2021JC018067](https://doi.org/10.1029/2021JC018067), 2022.

750 Pontes, G.M., Menviel, L.: Weakening of the Atlantic Meridional Overturning Circulation driven by subarctic freshening  
751 since the mid-twentieth century. *Nature Geoscience*, 17, 1291–1298. <https://doi.org/10.1038/s41561-024-01568-1>, 2024

752 Reichl, B. G. and Hallberg, R.: A simplified energetics based planetary boundary layer (ePBL) approach for ocean climate  
753 simulations., *Ocean Modelling*, 132, 112–129, <https://doi.org/10.1016/j.ocemod.2018.10.004>, 2018.

754 Reagan, James R., Boyer, Tim P., García, Hernán E., Locarnini, Ricardo A., Baranova, Olga K., Bouchard, Courtney, Cross,  
755 Scott L., Mishonov, Alexey V., Paver, Christopher R., Seidov, Dan, Wang, Zhankun, Dukhovskoy, Dmitry (2023). *World*  
756 *Ocean Atlas 2023. Salinity and Temperature*. NOAA National Centers for Environmental Information. Dataset.  
757 <https://doi.org/10.25921/va26-hv25>. Accessed October 2025.

758 Risaro D. B., Chidichimo M. P., Piola A. R.: Interannual Variability and Trends of Sea Surface Temperature Around  
759 Southern South America, *Frontiers in Marine Science*, 9, <https://www.frontiersin.org/articles/10.3389/fmars.2022.829144>,  
760 2022.

761 Rocha, C. B., Silveira, I. C. D., Castro, B. M., and Lima, J. A. M.: Vertical structure, energetics, and dynamics of the Brazil  
762 Current System at 22°S–28°S, *Journal of Geophysical Research: Oceans*, 119, 52–69,  
763 <https://doi.org/10.1002/2013JC009143>, 2014.

764 Rodrigues, R. R., Taschetto, A. S., sen Gupta, A., & Foltz, G. R.: Common cause for severe droughts in South America and  
765 marine heatwaves in the South Atlantic. *Nature Geoscience*, 12, 620–626. <https://doi.org/10.1038/s41561-019-0393-8>,  
766 2019.

767 Ross, A. C., Stock, C. A., Adcroft, A., Curchitser, E., Hallberg, R., Harrison, M. J., Hedstrom, K., Zadeh, N., Alexander, M.,  
768 Chen, W., Drenkard, E. J., du Pontavice, H., Dussin, R., Gomez, F., John, J. G., Kang, D., Lavoie, D., Resplandy, L.,  
769 Roobaert, A., Saba, V., Shin, S.I., Siedlecki, S., and Simkins, J.: A high-resolution physical-biogeochemical model for  
770 marine resource applications in the Northwest Atlantic (MOM6-COBALT-NWA12 v1.0), *Geoscientific Model*  
771 *Development Discussions*, 2023, 1–65, <https://doi.org/10.5194/gmd-2023-99>, 2023.

772 Schiller, A. and Ridgway, K. R.: Seasonal mixed-layer dynamics in an eddy-resolving ocean circulation model, *Journal of*  
773 *Geophysical Research: Oceans*, 118, 3387–3405, <https://doi.org/10.1002/JGRC.20250>, 2013.

774 Servain, J., Busalacchi, A., McPhaden, M., Moura, A., Reverfdin, G., Vianna, M., and Zebiak, S.: A pilot research moored  
775 array in the tropical Atlantic (PIRATA), *Bulletin of The American Meteorological Society*, 79, 2019–2032,  
776 [https://doi.org/10.1175/1520-0477\(1998\)079<2019:APRMAI>2.0.CO;2](https://doi.org/10.1175/1520-0477(1998)079<2019:APRMAI>2.0.CO;2), 1998.

777 Song, H., Marshall, J., McGillicuddy, D. J., and Seo, H.: Impact of current-wind interaction on vertical processes in the  
778 Southern Ocean. *Journal of Geophysical Research: Oceans*, 125, e2020JC016046. <https://doi.org/10.1029/2020JC016046>,  
779 2020

780 Stock, C. A., Pegion, K., Vecchi, G. A., Alexander, M. A., Tommasi, D., Bond, N. A., Fratantoni, P. S., Gudgel, R. G.,  
781 Kristiansen, T., O’Brien, T. D., Xue, Y., and Yang, X.: Seasonal sea surface temperature anomaly prediction for coastal  
782 ecosystems, *Progress in Oceanography*, 137, 219–236, <https://doi.org/10.1016/j.pocean.2015.06.007>, 2015.

783 Valerio, A. M., Kampel, M., Ward, N. D., Sawakuchi, H. O., Cunha, A. C., and Richey, J. E.: CO<sup>2</sup> partial pressure and fluxes  
 784 in the Amazon River plume using in situ and remote sensing data, *Continental Shelf Research*, 215, 104–348,  
 785 <https://doi.org/10.1016/J.CSR.2021.104348>, 2021.

786 Wright, D. G.: An Equation of State for Use in Ocean Models: Eckart's Formula Revisited, *Journal of Atmospheric and*  
 787 *Oceanic Technology*, 14, 735 – 740,  
 788 [https://doi.org/https://doi.org/10.1175/1520-0426\(1997\)014<0735:AEOSFU>2.0.CO;2](https://doi.org/https://doi.org/10.1175/1520-0426(1997)014<0735:AEOSFU>2.0.CO;2), 1997.

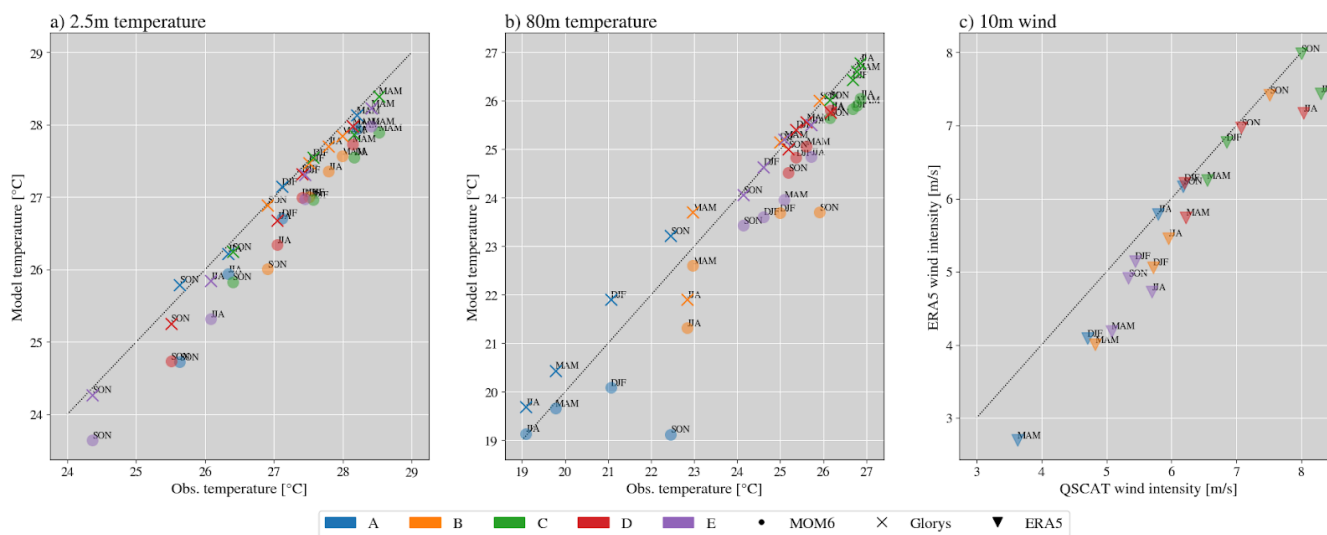
789 Wunsch, C. and Ferrari, R.: VERTICAL MIXING, ENERGY, AND THE GENERAL CIRCULATION OF THE OCEANS,  
 790 <https://doi.org/10.1146/annurev.fluid.36.050802.122121>, 36, 281–314,  
 791 <https://doi.org/10.1146/ANNUREV.FLUID.36.050802.122121>, 2004.

792 Zsoter, E., Harrigan, S., Barnard, C., Wetterhall, F., Ferrario, I., Mazzetti, C., Alfieri, L., and Salamon, P. and Prudhomme, C.:  
 793 River discharge and related historical data from the Global Flood Awareness System. v3.1.,  
 794 <https://doi.org/10.24381/cds.a4fdd6b9>, accessed 03 November 2023, 2021.

795 Zweng, M., Reagan, J., Seidov, D., Boyer, T., Locarnini, R., Garcia, H., Mishonov, A., Baranova, O., Paver, C., and Smolyar,  
 796 I.: *World Ocean Atlas 2018 Volume 2: Salinity*, 2019.

797

## 798 Supplementary material



799

800 Supplementary figure 1: As in Figure 5: Seasonal 2.5-m and 80-m temperatures and 10-m winds, compared against  
 801 observations. The graphs display the temperature at 2.5 m (a) and 80 m (b) for the model and reanalysis compared to  
 802 PIRATE buoy observations. In (c), the atmospheric forcing for the model, 10-m wind from ERA5, compared to QSCAT  
 803 satellite observation (Hoffman and Leidner, 2005). Colors distinguish the buoy sites from A to E. The model data is

804 obtained with the  $z^*$  vertical coordinate and marked with circles, extending from 1997 to 2017. The reanalysis from Glorys  
805 takes crosses and ERA5 triangles. The seasons are named as DJF, MAM, JJA, and SON.  
806